VOLCANICA Article in Press

This is an uncorrected proof, meaning that this manuscript has not been copyedited or formatted according to Volcanica's styles and standards. In turn, this means that article content, including text, may still change prior to final publication. Although articles in press do not have all bibliographic details available yet, they can be cited using the year of online publication and the DOI, as follows: author(s)(year), article title, Volcanica, DOI.

Natale, J., Falasconi, A., Grillo, T. O., Bevilacqua, A., Buono, G., Favalli, M., Fornaciai, A., Frontoni, A., Giordano, G., Intrieri, E., Nave, R., Pappalardo, L., Vona, A. and Di Traglia, F. (2026) "Volcaniclastic deposit failure as a source of pyroclastic density currents at Vesuvius during the 1944 eruption", *Volcanica*, 9(2). doi: 10.30909/vol/thmt5335.

article in press

Volcaniclastic deposit failure as a source of pyroclastic density currents during the 1944 eruption of Vesuvius

Jacopo Natale[1,2], Alessia Falasconi[1], Teresa Oreade Grillo[3], Andrea Bevilacqua[4], Gianmarco Buono[1], Massimiliano Favalli[4], Alessandro Fornaciai[4], Alessandro Frontoni[5,3], Guido Giordano[3,1], Emanuele Intrieri[6], Rosella Nave[1], Lucia Pappalardo[1], Alessandro Vona[3], Federico Di Traglia[1,6,7*]

[1] Istituto Nazionale di Geofisica e Vulcanologia (INGV), Sezione Osservatorio Vesuviano, Via Diocleziano 328, 80124, Napoli (Italia)
[2] Università degli Studi di Napoli "Federico II", Dipartimento di Scienze della Terra, dell'Ambiente e delle Risorse, Via Vicinale Cupa Cintia, 21, 80126 Napoli (Italia)
[3] Università degli Studi "Roma Tre", Dipartimento di Scienze, Largo San Leonardo Murialdo 1, 00146, Roma (Italia)
[4] Istituto Nazionale di Geofisica e Vulcanologia (INGV), Sezione Pisa, Via Battisti 53, 56125, Pisa (Italia)
[5] CNR - Istituto di Geologia Ambientale e Geoingegneria (IGAG), Monterotondo, Italy
[6] Università degli Studi di Firenze, Dipartimento di Scienze della Terra, Via La Pira 4, 50121, Firenze (Italia)
[7] National Research Council (CNR), Institute of Science, Technology and Sustainability for Ceramics (ISSMC), Via Granarolo 64, 48018, Faenza, Italy

[*] federico.ditraglia@ingv.it [corresponding author]
ORCiD (JN): 0000.0002.2186.3783
ORCiD (AF): 0009.0000.2338.5423
ORCiD (TOG): 0009.0004.3472.4848
ORCiD (AB): 0000.0002.0724.2593
ORCiD (GB): 0000.0002.5474.1985
ORCiD (MF): 0000.0002.7338.6069
ORCiD (AFO): 0000.0003.4829.4928
ORCiD (AFR): 0000.0002.9034.2068
ORCiD (GG): 0000.0002.5819.443X
ORCiD (EI): 0000.0002.9227.4409
ORCiD (RN): 0000.0002.4091.9404
ORCiD (LP): 0000.0002.9187.252X
ORCiD (AV): 0000.0002.5483.5623
ORCiD (FeDiT): 0000.0001.5869.0743

Keywords: Deposit-Derived Pyroclastic Density Currents; Vesuvius; Physical Volcanology; Digital Elevation Models; Violent Strombolian; Volcanic Eruption

Article in press

Abstract

Pyroclastic density currents (PDCs) are among the most lethal volcanic phenomena and are mainly generated by column collapse, lateral blasts, or dome failure. An additional but still poorly constrained hazard is represented by PDCs produced by the collapse of hot volcaniclastic deposits. Here we investigate deposit-derived (dd) PDCs emplaced during the 1944 eruption of Vesuvius (Italy). We integrate historical literature, contemporary written and photographic sources, and new field observations with a reconstruction of the pre-eruptive topography based on vintage aerial photographs and digital elevation models. Our results show that the pre-eruptive crater geometry exerted a primary control on deposit accumulation, failure mechanisms, and runout behaviour. Volume–area relationships indicate failure mechanisms broadly consistent with translational, near-planar collapse. Individual dd-PDCs reached volumes of up to ~3x10^6 m^3 and runout distances of ~1–1.5 km, ranking among the largest PDCs associated with sustained lava fountaining and highlighting an underestimated hazard capable of affecting areas up to 2 km from the vent.

Riassunto

Le correnti piroclastiche di densità (*pyroclastic density currents,* PDCs) sono tra i fenomeni vulcanici più letali e si originano principalmente dal collasso della colonna eruttiva, da esplosioni laterali o dal collasso di duomi lavici. Un ulteriore pericolo, ancora poco vincolato, è rappresentato dalle PDCs generate dal collasso di depositi vulcanici caldi. In questo studio analizziamo le PDCs derivate da deposito (*deposit-derived*, dd-PDCs) emesse durante l'eruzione del 1944 del Vesuvio (Italia). Il lavoro integra fonti storiche scritte e fotografiche, nuove osservazioni di terreno e la ricostruzione della topografia pre-eruttiva mediante fotografie aeree storiche e modelli digitali del terreno. I risultati mostrano che la geometria del cratere pre-eruttivo ha controllato l'accumulo dei depositi, i meccanismi di collasso e le distanze di propagazione. Le relazioni volume–area indicano collassi dominati da scivolamento planare. Le singole dd-PDCs hanno raggiunto volumi fino a ~3x10^6 m^3 e runout di ~1–1,5 km, collocandosi tra i più grandi PDCs associati a fontane di lava sostenute ed evidenziando un pericolo vulcanico spesso sottostimato fino a 2 km dalla zona di emissione.

Introduction

article in press

Pyroclastic density currents (PDCs) generated by gravitational collapse encompass a broad spectrum of processes involving the failure of hot volcanic materials, ranging from coherent lava domes and lava flows to recently emplaced volcaniclastic deposits (Branney and Kokelaar, 2002; Giordano et al., 2024). Within this spectrum, deposit-derived pyroclastic density currents (dd-PDCs) originate from the collapse of hot, unconsolidated to partially welded volcaniclastic accumulations, such as spatter blankets, proximal fallout deposits, crater-rim accumulations and clastogenic lava deposits (Risica et al., 2022; Di Traglia et al., 2026). Unlike classical block-and-ash flows, which result from the fragmentation of coherent lava bodies during dome or lava-flow collapse (Sato et al., 1992; Calder et al., 2002), dd-PDCs are generated by the remobilisation of weakly consolidated volcaniclastic material. The distinction is therefore primarily genetic rather than depositional, although differences in componentry and internal architecture commonly reflect the contrasting nature of the source material (Alvarado et al., 2023). Despite these differences, both processes belong to the broader family of gravity-induced PDCs, in which slope failure, rather than direct explosive fragmentation, is the primary mechanism controlling flow generation (Sato et al., 1992; Calder et al., 2002; Stinton et al., 2014; Harnett and Heap, 2021; Di Traglia et al., 2023a, 2024, 2025, 2026).

Deposit-derived PDCs can transport volumes ranging from 10^3 to 10^7 m^3 and travel several kilometres from their source while maintaining extremely high temperatures. This poses a significant risk to individuals residing near, working on, or visiting active volcanoes (Alvarado et al., 2023; Di Traglia et al., 2023a, 2026). Once considered exceptional phenomena, dd-PDCs are now recognised as relatively common under specific eruptive and geomorphological conditions, particularly during phases involving the accumulation of coarse proximal material (such as spatters) or lava emplacement on steeply sloping depositional surfaces (Di Traglia et al., 2026). Failures of this type have been directly observed or inferred from stratigraphic and geomorphological records at numerous volcanoes worldwide, including Fuego in Guatemala (Davies et al., 1978; Albino et al., 2020; Lerner et al., 2022; Risica et al., 2022; Charbonnier et al., 2023); Ngauruhoe in New Zealand (Nairn and Self, 1978; Lube et al., 2007); Arenal (Alvarado and Soto, 2002; Cole et al., 2005) and Rincón de la Vieja (Baez et al., 2024) in Costa Rica; Etna (Calvari and Pinkerton, 2002; Behnke et al., 2008; Norini et al., 2009; Andronico et al., 2018; Zuccarello et al., 2025; Costa and Viccaro, 2026) and Stromboli (Pioli et al., 2008; Di Roberto et al., 2014; Calvari et al., 2016, 2020; Salvatici et al., 2016; Di Traglia et al., 2018, 2023a, 2024, 2025; Giordano and De Astis, 2021; Casalbore et al., 2022, 2025; Bevilacqua et al., 2026; Neri et al., 2026; Corna et al., 2026) in Italy; Fuji and Aso in Japan (Yamamoto et al., 2005; Miyabuchi et al., 2006); Tungurahua in Ecuador (Kelfun et al., 2009; Douillet et al., 2013; Bernard et al., 2014); and Llaima in Chile (Romero et al., 2021). Focusing on the contemporary eruptive state (2002–2024), a significant disparity is observed between the triggers of PDCs at Stromboli. Within this interval,

article in press

eleven major crater-rim failures and associated dd-PDCs occurred during effusive or sustained Strombolian activity. In contrast, only five PDCs were generated by column collapsing during paroxysmal (mafic Vulcanian) explosions (Rosi et al., 2006; Pistolesi et al., 2011; Giordano and De Astis, 2021; Civico et al., 2024; Casalbore et al., 2022, 2025). These observations highlight that the hazard posed by dd-PDCs may peak during eruptive phases that are commonly perceived as being of low to moderate intensity, when preparedness and risk awareness are often reduced (Turchi et al., 2026).

Dd-PDCs can be broadly grouped into two principal end-member mechanisms that reflect different modes of destabilisation of hot proximal material. The first end-member corresponds to failures driven by magma thrust, here referred to as Arenal-type dd-PDCs (Alvarado and Soto, 2002). In this configuration, instability develops through repeated lava effusion, overflow or shallow intrusion, which progressively loads, oversteepens or undercuts crater rims and proximal slopes. Consequently, failure is closely coupled with magma dynamics and sustained effusive activity, and may occur repeatedly over short timescales, producing multiple dd-PDCs of limited to moderate volume (Alvarado and Soto, 2002; Cole et al., 2005). The second end-member corresponds to failures resulting from the gravitational collapse of hot proximal deposits once critical stability thresholds are exceeded, here referred to as Fuego-type dd-PDCs (Di Traglia et al., 2026). In this case, instability is primarily controlled by the rapid accumulation of fountain-derived or coarse proximal material on a pre-existing substrate. This substrate may consist either of mechanically resistant deposits that remain stable or of previously accumulated volcaniclastic material that can become incorporated into the collapsing mass, thereby contributing to the final collapse volume, as observed during the 3 June 2018 event at Fuego (Risica et al., 2022; Charbonnier et al., 2023). Failure occurs when the load imposed by the newly emplaced deposits exceeds the resistance of the underlying surface or exploits mechanical heterogeneities within the accumulating deposit pile itself. Fuego-type dd-PDCs are commonly associated with Strombolian to violent Strombolian eruptive activity. These events are typically characterised by abrupt collapses that may involve large volumes and whose magnitude is strongly influenced by summit morphology and deposit architecture (Albino et al., 2020; Risica et al., 2022; Charbonnier et al., 2023; Di Traglia et al., 2026).

Within this spectrum, the 1944 eruption of Vesuvius represents a pivotal case study for exploring the processes governing the generation of dd-PDCs, their links with eruptive dynamics and summit morphology, and the implications of such phenomena for hazard assessment at persistently active volcanoes. Although their occurrence was documented in the detailed chronicle of Imbò (1949), these currents remain only partially understood, particularly with regard to the mechanisms responsible for their initiation and the parameters required for robust hazard evaluation (e.g. source area, flow extent and volume, runout distance). To address these gaps, we re-

article in press

examined Imbò's chronicle of the 1944 eruption together with contemporary photographic documentation, in order to clarify the relationship between eruptive phases and dd-PDC emplacement. Field investigations were complemented by the analysis of archival aerial imagery, which provided a basis for reconstructing pre- and post-eruptive summit morphology. In particular, orthophotogrammetric datasets from 1943 and 1954 were used to constrain the geomorphological evolution of the cone following the eruption, whereas quantitative estimates of deposit volumes were derived from DEM differencing between the 1943 surface and a modern high-resolution topographic dataset (2013).

article in press

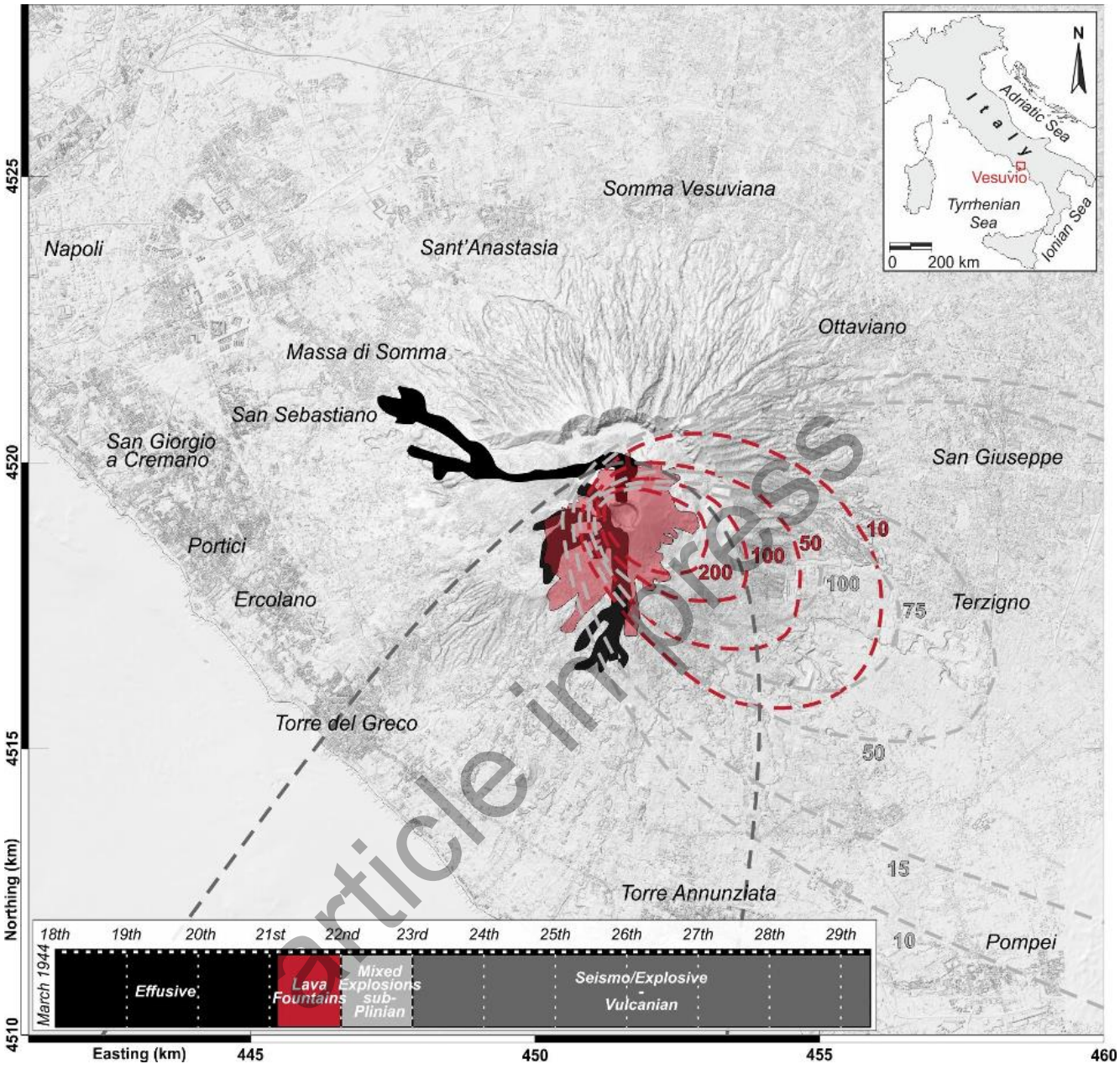

article in press

Figure 1: Digital Elevation Hillshade Model of the Somma–Vesuvius volcanic complex showing the distribution of deposits from the 1944 eruption: Phase 1 lava flows (black), Phase 2 lava-fountain fallout and hot avalanches (shaded red), and tephra fallout from Phases 3–4 (light grey ellipses), after Cole and Scarpati (2010). The bottom inset shows a simplified chronology of the eruption.

Historical eruptions and eruptive style at Vesuvius

Renowned worldwide for its Plinian and sub-Plinian activity (Sheridan et al., 1981; Rosi and Santacroce, 1983; Rosi et al., 1993; Cioni et al., 2008; Pensa et al., 2023; Falasconi et al., 2025), Vesuvius experienced its most recent eruptive cycle between 1631 and 1944. This period was characterised by persistent activity, including summit Strombolian explosions, sustained lava effusion, and episodic violent Strombolian and sub-Plinian eruptions (Arrighi et al., 2001; Scandone et al., 2008). Among these high-energy events, the classification of the 1822, 1906 and 1944 eruptions remains debated. Cioni et al. (2008) consider all three events to be violent Strombolian. Conversely, Arrighi et al. (2001) classified the 1822 and 1906 eruptions as sub-Plinian, while defining the 1944 eruption as violent Strombolian. In this study, we follow the classification proposed by Cole and Scarpati (2010), who interpret the 1944 eruption as a sub-Plinian event. Violent Strombolian and sub-Plinian eruptions were typically preceded by phases of rapid lava effusion and, in some cases, followed by short-lived periods of quiescence (Scandone et al., 2008). Mafic sub-Plinian eruptions at Vesuvius typically erupted volumes on the order of $\sim 10^7$ m³, with eruption columns reaching heights of ~10 km and were characterised by mass discharge rates of at least 10^6 kg s^{-1} (Arrighi et al., 2001; Cole and Scarpati, 2010). PDCs accompanied each of these three major eruptions. The 1822 eruption involved two crater-rim failures that generated dd-PDCs propagating eastwards (Monticelli and Covelli, 1823; Arrighi et al., 2001). Monticelli and Covelli (1823) reported that these currents occurred during both the early and late stages of the eruption and were consistently associated with lava effusion; they described the resulting deposits as “lava with incoherent debris”. The 1906 eruption produced several PDCs related to eruption column collapse (Bertagnini et al., 1991; Chester et al., 2015). During the 1944 eruption, both failures of hot proximal material, resulting in glowing avalanches and PDCs generated by partial column collapse were documented (Imbò, 1949; Hazlett et al., 1991; Cole and Scarpati, 2010).

The 1944 eruption and the associated dd-PDCs

The most recent eruption of Vesuvius, the mafic (K-phonotephritic to K-tephrites; Marianelli et al., 1999; Pappalardo et al., 2014) event of March 1944, has been extensively investigated from multiple perspectives, including magma composition and evolution (Santacroce, 1987; Fulignati et al., 2004; Marianelli et al., 2005; Pappalardo et al., 2014; Cubellis et al., 2016) as well as eruptive processes and dynamics (Cioni et al., 2008; Arzilli et al., 2026). More recent studies have combined petrological and seismic indicators to develop monitoring strategies aimed at identifying transitions towards more violent eruptive behaviour (Pappalardo et al., 2014). A

article in press

comprehensive reconstruction of the 1944 eruption was presented by Cole and Scarpati (2010), who integrated contemporary observations with new field data and extensively exploited eyewitness accounts compiled by Giuseppe Imbò, then Director of the Osservatorio Vesuviano (Imbò, 1949), together with Parascandola's (1945) reports on tephra accumulation in surrounding villages. In the following section, we summarise the main phases of the March 1944 eruption as documented in Imbò's chronicles. Prior to the onset of the 1944 eruption, Vesuvius had experienced more than three decades of persistent intracrateric effusive and Strombolian activity. The ~600-m-deep crater excavated during the 1906 eruption had been progressively infilled by lava erupted since July 1913, and several lava overflows from the summit lava platform occurred since 1929. During the final days preceding the eruption, a small intracrater cone on the eastern side collapsed during the night of 12–13 March 1944, while weak explosive activity on 14 March briefly reopened the conduit, which became obstructed again following further collapse on the morning of 18 March, immediately before the onset of the main eruptive phase. Following the end of the 1944 eruption, the conduit remained obstructed, marking the beginning of the prolonged period of closed-conduit quiescence that continues to the present day.

Phase 1 – Effusive phase (Figs. 1, 2b). The eruption began at 16:30 on 18 March with a mild explosion that partially destroyed the intracrater scoria cone. Two lava flows were emitted immediately afterwards, one advancing towards the south-east and the other initially moving northwards before being deflected westward at the base of the cone by Mt Somma. Explosive activity progressively intensified, producing jets of lapilli and scoria up to ~150 m above the crater rim. Lava effusion increased on 20–21 March, generating additional flows, including one that advanced north-westward towards San Sebastiano al Vesuvio and Massa di Somma at velocities of 50–300 m h^{-1} (Imbò 1949), inundating large parts of both settlements by late March 21st. By the end of this phase, approximately 21 × 10^6 m^3 of lava had been emplaced, with flow fronts reaching ~350 m a.s.l. on the south-eastern flank and ~140 m above sea level (a.s.l.) on the northern flank by 22 March (Fig. 1).

Phase 2 – Lava fountaining (i.e. Violent Strombolian) (Fig. 2c; Table 1). At 17:15 on 21 March, activity shifted abruptly to a Violent Strombolian regime, with jets reaching heights of up to ~2 km and the eruptive columns exceeding 4 km (Imbò, 1949). Lava effusion persisted, albeit at markedly reduced discharge rates. Eight episodes of lava fountaining were recorded, the final one lasting nearly five hours. According to Imbò (1949), each episode terminated with the emission of acoustic waves accompanied by a luminous arc. Spatter bombs and lapilli accumulated unevenly around the crater rim, attaining maximum preserved thicknesses in the eastern sector (Fig. 2a). The eruptive column was dispersed predominantly towards the east and south-east (Fig. 1), producing widespread fallout ranging from fine lapilli to blocks. At least 17 × 10^6 m^3 of eruptive material were emplaced during this phase (Cole and Scarpati, 2010). By the end of the Violent Strombolian phase, the summit morphology

article in press

had been extensively remodelled. The upper cone was characterised by multiple collapse scars generated by the remobilisation of deposits emplaced during Phase 2, many of which extended upslope to the crater rim, while a pronounced depression developed on the northern flank (Imbò, 1949).

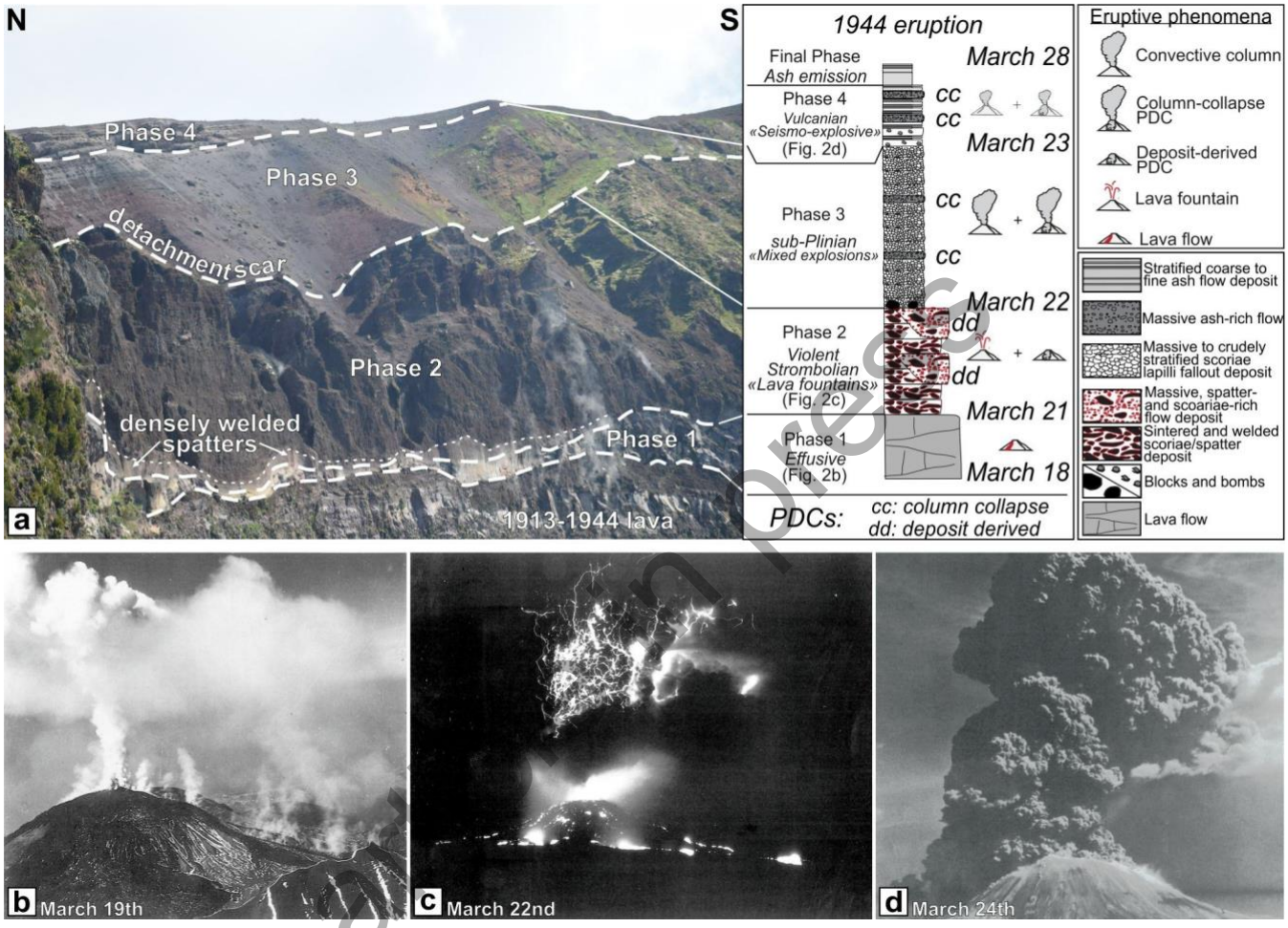

Figure 2: Overview of the main eruptive phases of the 1944 eruption, as inferred from field observations and contemporaneous photographs. (a) Interpreted field photographs showing a representative type section with the corresponding simplified stratigraphic log. (b) Aerial photograph of the Phase 1 lava flow along the northern flank of the Vesuvius. (c) Night-time photograph of lava fountains during Phase 2 and incandescent deposits at the base of the cone. (d) Aerial photograph of Phase 4 characterised by ash explosions and minor PDCs.

Phase 3 – Mixed explosive activity (i.e. sub-Plinian) (Fig. 1). This phase began shortly after 12:00 on 22 March and was characterised by the onset of sustained, dark ash-rich eruptive columns, the formation of a new summit crater, and the generation of column-collapse PDCs. An initial eruptive column, rich in dense lava fragments and

juvenile material, was followed by a temporary decline in activity. Subsequent crater collapse further modified the summit morphology before activity resumed at around 21:00, when two vents began emitting reddish ash-rich columns that persisted into 23 March. This was the climactic phase of the eruption, producing widespread tephra fallout (Fig. 1), with ash reported several hundred kilometres from the volcano, including at Bari (210 km) and Berat, Albania (470 km; Lazzari, 1947). Overall, this phase resulted in the emplacement of at least 237×10^6 m³ of eruptive material (Cole and Scarpati, 2010).

Phase 4 – Seismic–explosive phase (i.e. Vulcanian) (Figs. 1, 2d). The fourth phase, characterised by Vulcanian-style activity, began at 14:00 on 23 March and marked a transition from high-intensity explosions to sustained ash emission. Activity was dominated by intermittent ash columns generated by repeated conduit obstruction and clearing, accompanied by strong seismicity (Fig. 2d). On 23 March, a white ash blanket was deposited across the summit, while ash dispersal continued over the following days. On 26 March, coarse proximal ejecta accumulated upwind near the crater, whereas ash emission persisted downwind. Explosive activity became sporadic on 27–28 March, and both eruptive and seismic signals ceased on 29 March. Minor ash emissions continued until 7 April, attributed by Imbò (1949) to partial collapses of the inner crater walls. During this phase, at least 4.2×10^6 m³ of material were emplaced, although this figure is likely an underestimate due to the extensive erosion of the deposits (Cole and Scarpati, 2010).

Imbò (1949) reported the occurrence of what today we define as dd-PDCs, between 18 and 29 March 1944, mainly during the Phase 2 that followed the initial effusive Phase 1. He referred back then to these currents as "pseudo-flows", the same term used for dd-PDCs produced during the 1930 eruption of Stromboli (Imbò, 1928; Rittmann, 1931; Abbruzzese, 1936; Di Roberto et al. 2014; Salvatici et al. 2016), and clearly distinguished them from PDCs generated by eruptive column collapse during the Phase 3 and the subsequent Phase 4. Hazlett et al. (1991), instead, attributed many of the 1944 avalanches to a short-lived episode of intense seismicity during the Phases 3-4, an interpretation later reiterated by Cagnoli et al. (2015). In his account, Imbò (1949) distinguished two main types of PDCs:

(1) Pseudo-lava flows (*pseudo-colate*; Imbò 1949) generated by the downslope mobilisation of still hot, partially molten material during Phase 2, whose agglutination and subsequent movement were facilitated by pre-existing topographic controls. They propagated predominantly along the western flank, with the largest reaching elevations of ~700 m a.s.l. On the basis of their origin and dynamics, these flows are here classified as dd-PDCs and include part of the "avalanches" described by Hazlett et al. (1991). Comparable behaviour had already been documented by Imbò during the 1930 Stromboli eruption, where he described unstable masses of incandescent material descending the slopes "like a lava flow laden with ash and material entrained by the advancing mass" (Imbò, 1928).

article in press

(2) Small nuées ardentes (*nubi ardenti in miniatura*; Imbò 1949), generated by partial collapses of the eruptive column during Phase 3 and, to a lesser extent, Phase 4 (Cole and Scarpati, 2010). These PDCs resemble those described by Lacroix for the 1906 eruption, although they differ from large-scale column-collapse flows (Lacroix, 1906). They exhibited no preferred propagation direction and advanced at estimated velocities of 30–50 m sec^{-1}. According to Imbò (1949), the most substantial event occurred on the morning of 24 March, propagated southwards, and involved approximately 3×10^5 m^3 of solid material. On the basis of their source mechanism and physical characteristics, these currents are here referred to as column-collapse PDCs (Branney and Kokelaar, 2002).

Methods

This study integrates detailed field investigations with photogrammetric reconstruction of pre- and post-eruptive topography to characterise dd-PDCs generated during the 1944 eruption of Vesuvius. Field observations were used to constrain the stratigraphy, geometry and degree of welding of proximal Phase 2 fallout deposits, and to identify dd-PDCs at medial and distal distances. These datasets were combined with high-resolution digital elevation models (DEMs) derived from archival aerial photographs to reconstruct flow paths, delineate source areas (detachment scars) and depositional geometries, and to quantify key morphometric parameters, affected areas and mobilised volumes.

Field investigations

Fieldwork was carried out with two main objectives: (i) to characterise proximal deposits in terms of stratigraphy, geometry and degree of welding, and (ii) to analyse PDC deposits, with particular emphasis on their spatial distribution and stratigraphic relationships with other deposits emplaced during the 1944 eruption. Stratigraphic sections along the crater rim were examined to document the texture and grain-size characteristics of proximal materials. Special attention was paid to bed dip and welding intensity, which were assessed macroscopically in both the ash matrix and the coarse fraction. Each outcrop was systematically described and photographed.

Welding intensity was evaluated on the basis of fabric and textural variations, clast morphology, and clast aspect ratio. The latter was quantified by measuring five to six representative clasts at each site along perpendicular X and Y axes. This approach follows the methodology proposed by Carey et al. (2008) and is summarised in Table 1. The identification of dd-PDCs was based on the integration of field observations with the descriptions and maps provided by Imbò (1949) and Hazlett et al. (1991). These sources were critically re-evaluated and refined through systematic surveys of the cone flanks at medial and distal distances. Field-based interpretations were subsequently

article in press

used to guide the mapping of dd-PDC deposits and their detachment scars on DEMs and orthophotos, forming the basis for morphometric and volumetric analyses.

Table 1: Nomenclature used in descriptions of welding degree of the Vesuvius 1944 proximal deposits. For each welding degree, attributes of both clasts and matrix are described (from Carey et al. 2008)

Welding degree	Attribute of welding	
	Matrix	**Clast**
Dense	Glassy eutaxitic textures, no obvious pyroclastic texture. No void space between clasts	Ghost-like outlines of clasts with minor relic vesicularity. Extremely flattened flames
Moderate	Clasts sintered together. No void space between clasts	Elongated clasts with flattened vesicles, outlines of clasts. Some relic vesicularity of clasts still recognizable
Slight	Clasts sintered together, however clastic texture	Firmly sintered edges, flattened clasts. Edges of clasts still partly recognizable
Tack	Loose, unconsolidated with void space	Sintered edges, ragged form of pumices. Rounded undeformed vesicles
No welding	Loose, unconsolidated	Undeformed, original ragged form of pumices

article in press

Dataset and photogrammetric processing of vintage aerial photographs

To reconstruct pre- and post-eruptive topography, we used aerial photographs acquired in 1943 and 1954 by the Istituto Geografico Militare (IGM, Authorization 7270, dated 17/02/2026). Among the available datasets, these two surveys were selected because they respectively document pre-eruptive and post-eruptive conditions and provide the best compromise in terms of spatial coverage, photograph overlap (60–90%), cloud disturbance and the availability of suitable control points (Fig. 3). The 1943 dataset comprises 79 photographs acquired in July 1943 using a Zeiss camera with a 200.72 mm focal-length lens, distributed along four flight stripes: two flown at ~5 km elevation (35 photographs) and two at ~3.8 km (44 photographs), yielding an average scale of ~1:18,000.

The 1954 dataset includes 47 photographs acquired at ~6 km elevation along four N–S-oriented stripes using a Fairchild camera with a 153.01 mm focal-length lens, corresponding to a scale of ~1:35,000 (Fig. 3).

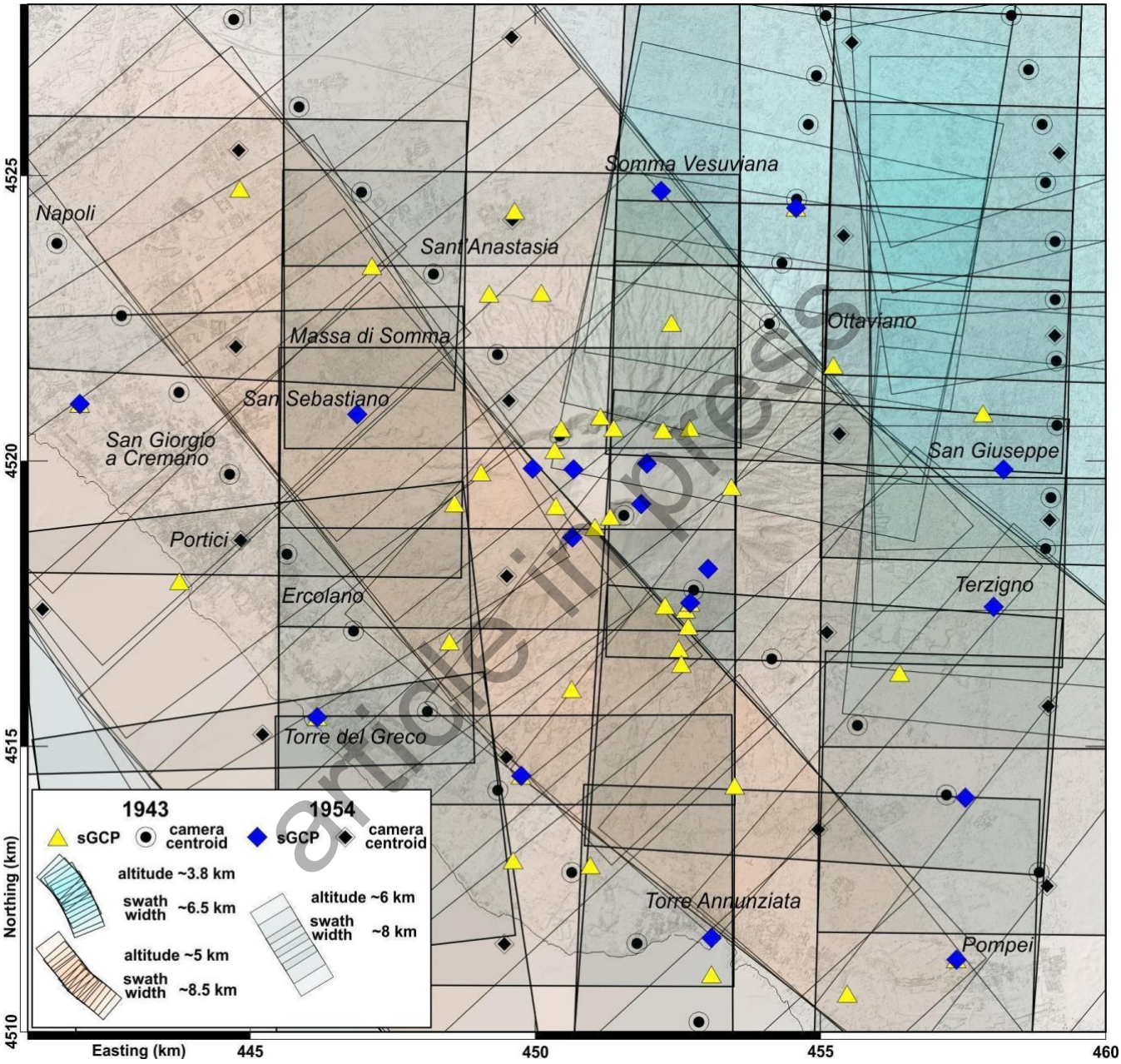

article in press

Figure 3: Map of 1943 and 1954 IGM flights coverage of the used aerial photographs. In the bottom left corner, the footprint (swath) of the photographs is indicated according to the corresponding flight elevation. Yellow triangles are the used sGCP (synthetic Ground Control Points). Coordinates WGS84 UTM 33 N.

Photogrammetric processing followed the workflow described by Natale et al. (2024) for aerial photographs of the same year. All processing was performed using Agisoft Metashape (v. 1.7.6) and a Structure-from-Motion approach, including: (a) pre-processing and masking of irrelevant or disturbed areas (e.g. sea surface, film defects, censored regions); (b) camera alignment and incremental optimisation of the sparse point cloud (Mayer et al., 2018; Natale et al., 2024); (c) identification and placement of synthetic Ground Control Points (50 for 1943 and 21 for 1954), with coordinates extracted from the LiDAR-derived DTM in WGS84 UTM 33, followed by additional optimisation; (d) generation, filtering and meshing of the dense point cloud; and (e) production of DEMs and orthomosaics.

Topographic change detection, morphometric analysis and volume estimation

Topographic changes associated with the 1944 eruption were quantified by comparing the 1943 historical digital surface model (hDSM) with the 1-m-resolution LiDAR-derived digital terrain model (DTM) surveyed in 2009-2012, and published in 2013 by the Città Metropolitana di Napoli, which was used as the present-day reference surface. As the LiDAR dataset represents bare-earth topography, it provides a suitable reference for geomorphological comparison with the historical photogrammetric model. Topographic changes were assessed by generating a DEM of Difference (DoD) between the 1943 hDSM and the 2013 LiDAR-derived DTM, which represents the cumulative morphological changes affecting the summit area since the 1944 eruption. Residual misalignment between DEMs may introduce artificial elevation differences (Δh) unrelated to actual topographic changes (Fornaciai et al., 2010; Di Traglia et al., 2018, 2020, 2022). To minimise these artefacts, the DEMs were co-registered using stable areas where no significant geomorphological changes were expected. The co-registration workflow comprised five steps: (i) preliminary comparison of the DEMs to identify stable reference areas and sectors affected by genuine topographic changes; (ii) calculation of the initial root mean square (RMS) elevation difference over the selected stable areas; (iii) optimisation of the co-registration parameters using the MINUIT minimisation algorithm; (iv) registration of the slave DEM to the master DEM using the optimised transformation parameters; and (v) estimation of the residual RMS elevation difference from independent stable areas to quantify the co-registration error. The volume of material emplaced or removed between the two surveys was calculated from the DoD according to

$$V = \sum_{i=1}^{n} (\Delta x)^2 \Delta z_i$$

article in press

where Δx is the DEM grid spacing and Δzi is the elevation change measured in the i-th grid cell (Fornaciai et al., 2010; Di Traglia et al., 2018, 2020, 2022). The total volume change was obtained by summing the contributions of all grid cells within the selected area.

A conservative upper bound of the volumetric uncertainty was estimated by assigning the maximum residual elevation error to every grid cell:

$$ErrV,high = A\sigma\Delta Z$$

where (A) is the investigated area and ΔZ is the residual RMS elevation difference calculated from the independent stable areas. Consequently, the reported uncertainties represent conservative estimates and are expected to overestimate the actual error associated with the calculated volumes (Fornaciai et al., 2010; Di Traglia et al., 2018, 2020, 2022).

For the calculation of mobility parameters (Hayashi and Self, 1992; Calder et al., 1999), the average elevation of the 1944 crater rim (1171 m a.s.l.) was adopted as the reference elevation. Runout distance (L) was measured along the cumulative flow path from the mapped detachment area to the distal margin of each dd-PDC deposit. This approach accounts for the gravity-driven nature of the flows and avoids the bias associated with vent- or crater-centred distance measurements. Accordingly, the mobility index (H/L) was calculated using the vertical drop between the detachment area and the distal deposit margin, ensuring consistency between the height and runout measurements.

Results

The results integrate stratigraphic observations of proximal deposits with topographic and morphometric analyses derived from historical digital elevation models. Field data constrain the physical properties and instability conditions of Phase 2 deposits, while DEM-based analyses document morphological changes, detachment areas, flow paths and the spatial distribution, runout and volumes of deposit-derived pyroclastic density currents generated during the 1944 eruption of Vesuvius.

Morphological evolution of the cone

The 1944 eruption produced substantial morphological modifications to the Vesuvius cone, which, prior to the eruption, was dominated by the large crater formed in 1906. The shaded-relief image derived from the 1943

article in press

historical DSM (Fig. 4a) clearly delineates the rim of the 1906 crater and the lava platform that progressively infilled it following effusive activity after 1913 (Figs. 4a, 5a). A small intracrater scoria cone is visible near the centre of this platform. The southern flank preserves the 1906 lava-flow field, whereas lava flows emplaced between 1929 and 1944 dominate the northern and eastern sectors (Fig. 5a). Elsewhere, the flanks of the 1906 cone are characterised by well-developed erosion gullies incised into the ash deposits emplaced during the 1906 eruption (Figs. 4e, 5c). Overall, the cone exhibited a markedly convex-conical morphology, with steep slopes ranging from 30° to 45° (Fig. 5a). Additional features, including the eccentric vent formed in 1937 and the lava-flow lobes of the 1929 eruption extending beyond the Mt Somma rim, are more clearly visible in the 1943 orthomosaic (Fig. 4b, c). A photograph acquired from an RAF aircraft in January 1944 shows the lava platform surmounted by a degassing scoria cone (Fig. 4d). The western sector of the cone was not mantled by lava flows emplaced between 1929 and 1944 and therefore preserves the surface formed during the 1906 eruption, where proximal deposits display well-developed erosion gullies (Figs. 4e, f; 5c). In contrast, the northern and eastern sectors are mantled by younger lava flows, while the southern flank remains dominated by the 1906 lava field (Figs. 4b, 5a, c).

The morphological impact of the 1944 eruption is further expressed by the formation of a new crater during Phases 3 and 4. This crater occupies the south-western sector of the pre-existing 1906 crater and covers an area of approximately 2×10^5 m², less than half that of the 1906 crater (approximately 4×10^5 m²; Figs. 5b, 6a). Deposits emplaced during the 1944 eruption form radial morphological features along the cone slopes and are clearly visible in both the slope map derived from the post-eruptive DEM (Figs. 5b, d) and the 1954 orthomosaic (Fig. 6a). An aerial photograph acquired shortly after the end of the eruption shows remnants of Phase 2 deposits bordering collapse scars, together with the subterminal lava emission point that developed during Phase 1 on the north-eastern flank (Fig. 6c). The newly formed crater partially destroyed the lava platform that had developed between 1913 and 1944. In the western and south-western sectors, the rim of the 1944 crater largely coincides with that of the 1906 crater (Fig. 6d), whereas in the northern and eastern sectors parts of the 1906 crater rim and sections of the former lava platform are buried beneath deposits emplaced during the 1944 eruption. Consequently, the cone developed a more convex-conical morphology, with slope angles of 15–30° in the upper sector and 30–45° in the lower sector (Fig. 5b). The south-western flank experienced only minor slope changes relative to the other sectors (Figs. 5a, b; Fig. S1). However, localised convexities are present in correspondence with the collapse scars (Figs. 5b, d, 6). Thin blankets of scoria and ash characterise the western sector, whereas thicker accumulations occur on the eastern flank (Figs. 5d, 6c).

article in press

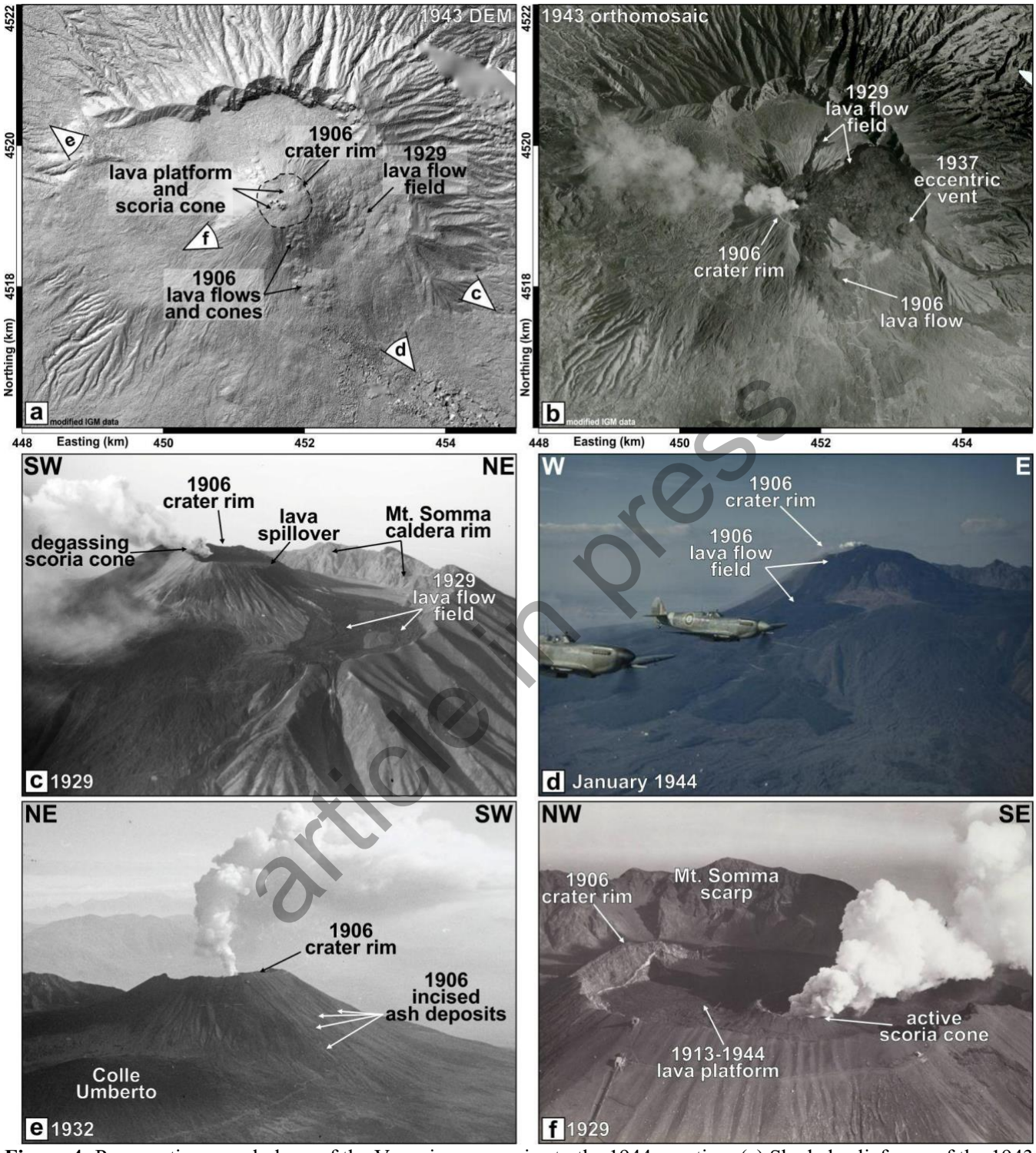

article in press

Figure 4: Pre-eruptive morphology of the Vesuvius cone prior to the 1944 eruption. (a) Shaded-relief map of the 1943 historical digital surface model (hDSM) reconstructed from IGM aerial photographs. Optical cones indicate the

approximate orientation and location of aerial photographs shown in c-f. (b) Orthomosaic generated from the 1943 IGM aerial photographs (Authorisation 7270, dated 17/02/2026). (c) Oblique aerial photograph acquired in 1929, looking northwest. (d) Oblique aerial photograph taken in January 1944 (credits to RAF). (e) Oblique aerial photograph acquired in 1932, looking southeast and showing the north-eastern flank. (f) Oblique aerial photograph from 1929 illustrating the lava platform and associated degassing plume from the conelet (IGM, 1929); the inner part of the 1906 crater and the summit station of the Vesuvius funicular are also visible.

article in press

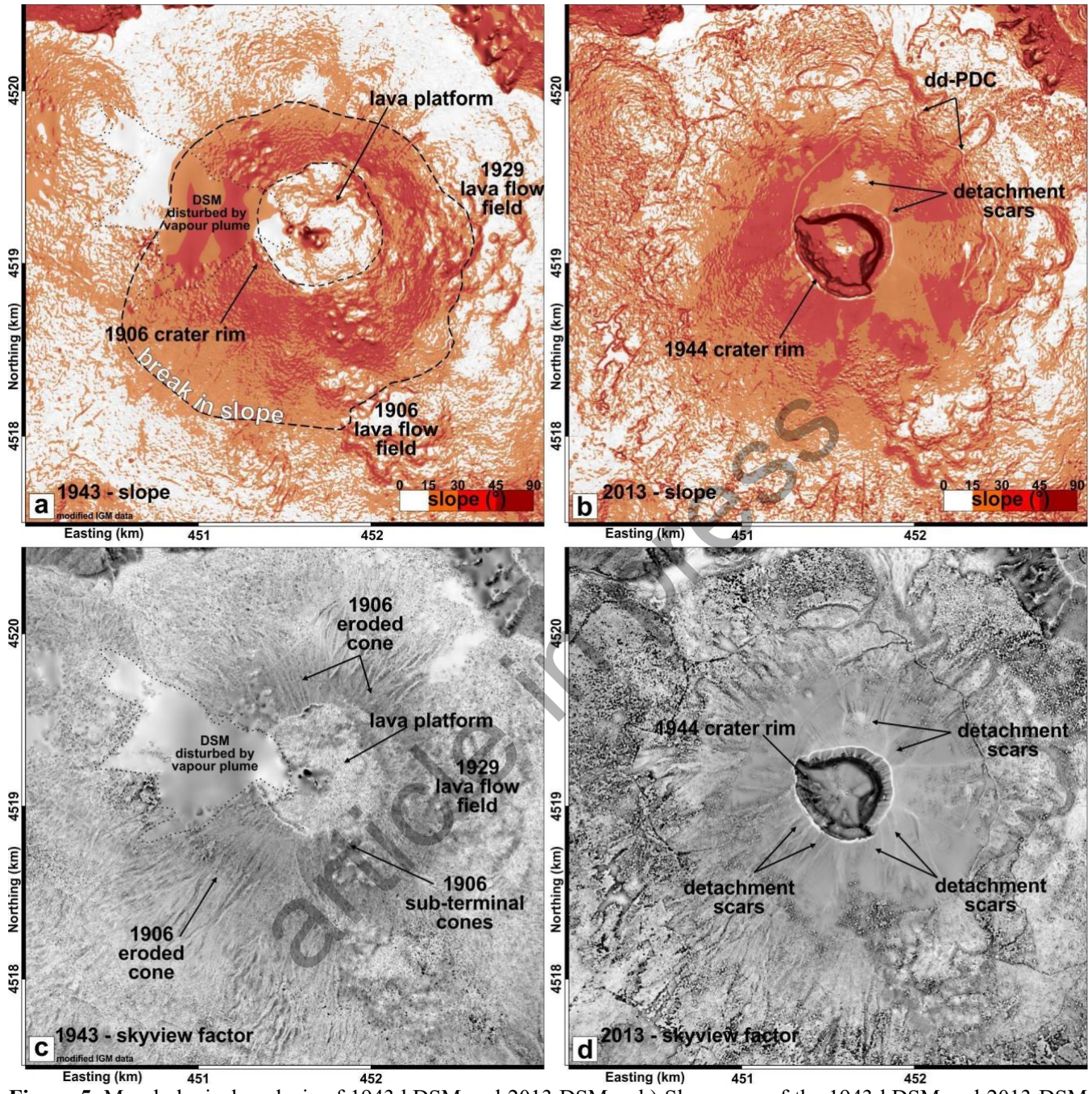

article in press

Figure 5. Morphological analysis of 1943 hDSM and 2013 DSM. a-b) Slope map of the 1943 hDSM and 2013 DSM showing the main features of the main cone prior and after the 1944 eruption; c-d) Skyview factor of the 1943 hDSM and 2013 DSM highlighting the complex morphologies due to erosive gullies and lava flow fields in 1943 and the numerous detachments scars of the 1944 eruption.

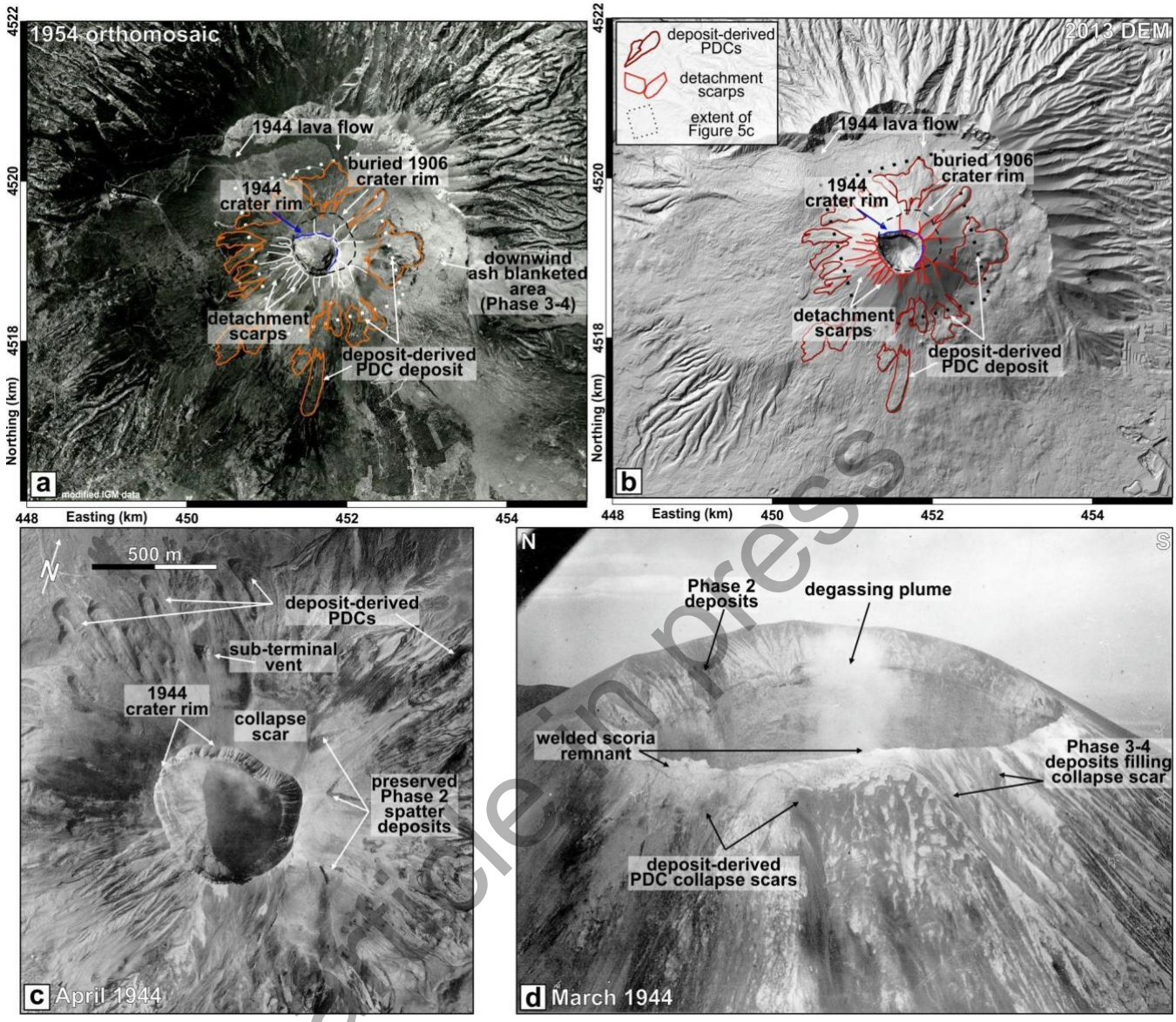

Figure 6: Post-eruptive morphology of the Vesuvius cone following the 1944 eruption. (a) 1954 orthomosaic derived from IGM aerial photographs (Authorisation 7270, dated 17/02/2026) showing the main post-eruptive morphological features, including dd-PDC detachment scars and deposits, the partially buried 1906 crater rim, and the northward-directed 1944 lava flow. (b) Shaded-relief image of the 2013 LiDAR-derived digital terrain model highlighting the distribution of dd-PDC deposits; the dashed rectangle indicates the approximate extent of panel (c). (c) Nadir aerial photographs acquired one month after the eruption (Imbò, 1949), showing the cone mantled by ash, with dd-PDC deposits and associated detachment scars visible on the northern and eastern slopes. (d) Oblique aerial photograph illustrating detachment scars along the western sector of the 1944 crater rim, subsequently infilled by ash from Phases 3 and 4.

Article in press

Stratigraphy and welding characteristics of deposits at the crater rim

Stratigraphic analysis shows that the northern and eastern sectors of the crater rim preserve an almost complete record of the 1944 eruption, comprising proximal successions exceeding 50 m in total thickness and including deposits from Phases 1 to 4 (Fig. 2a), consistent with the stratigraphic framework previously described by Cole and Scarpati (2010). In the northern sector, the thickest units correspond to the deposits of Phases 2 and 3, each reaching approximately 20–25 m, whereas Phase 4 deposits generally attain thicknesses of 3–5 m. In contrast, sectors where remnants of the 1906 crater rim are preserved lack deposits from Phases 3 and 4 and are instead dominated by Phase 1 and Phase 2 deposits resting directly on the pre-existing 1906 surface. Several representative stratigraphic sections of the Phase 2 succession were investigated along the crater rim and at the base of the cone (Fig. 7a). These deposits are dominated by lapilli, with subordinate juvenile bombs ranging from a few centimetres to several decimetres in diameter, many of which became flattened upon deposition to form spatter. Welding intensity was assessed macroscopically following the criteria of Carey et al. (2008) (Table 1), based on matrix texture, clast morphology, clast aspect ratio and clast–clast contacts. The Phase 2 succession exhibits marked vertical and lateral variations in welding intensity. At the base of the succession, a laterally continuous, densely welded spatter layer directly overlies the pre-existing lava surface (Fig. 7b). This facies is characterised by a glassy eutaxitic matrix lacking obvious pyroclastic texture, the absence of inter-clast void space, ghost-like clast outlines, extremely flattened juvenile clasts with high aspect ratios and only minor relic vesicularity. Above this basal unit, the succession comprises an irregular alternation of densely welded, moderately welded, slightly welded, tack-welded and non-welded spatter and lapilli beds, with repeated transitions over decimetre- to metre-scale intervals (Fig. 7c). Moderately welded facies are characterised by sintered clast contacts, elongated clasts with flattened vesicles and recognisable clast outlines, whereas slightly welded facies retain a clastic texture with only partially sintered clast margins. Tack-welded facies remain loose and unconsolidated, preserving inter-clast void space together with sintered clast edges and rounded, largely undeformed vesicles. Moderately welded deposits occur as stratified to massive beds and commonly alternate with slightly welded horizons, whereas tack- to non-welded reddish facies consist of poorly sorted scoriaceous deposits with abundant void space and angular clasts, locally containing unconsolidated ash-rich horizons in which some coarse clasts display incipient flattening. In the southern and western sectors, the preserved Phase 2 succession exhibits pronounced lateral variations in thickness, ranging from approximately 1 to 15 m, together with abrupt lateral changes in welding intensity over distances of only a few metres. This heterogeneous internal architecture is consistently observed along the southern crater rim and parts of the eastern flank. In these sectors, the basal part of the succession commonly comprises stratified to massive,

article in press

densely welded dark-brown spatter beds displaying ghost-like clast outlines, high clast aspect ratios, flattened vesicles and local rheomorphic fabrics (Fig. 7d). These facies typically occur immediately above the Phase 1 lava flows but may also be present higher within thicker Phase 2 successions (Fig. 7b). Polished slip surfaces are systematically observed within moderately to slightly welded intervals of the Phase 2 succession (Fig. 8a–c). They are most common along thinner crater-rim sections, where they locally bound small depressions, and are locally coated by thin veneers of welded ash. The surfaces are generally smooth and preserve well-developed slip striations (Fig. 8d-e). Along the crater rim, the striations are predominantly oriented parallel to the dip direction of the failure planes, indicating dominantly dip-slip displacement. The geometry of the detachment zones is variable: in some sectors it is defined by a single, planar failure surface, whereas elsewhere it results from several closely spaced fracture surfaces — including both open tensile fractures and polished slip surfaces — that together define a macroscopically continuous, concave detachment area. Individual failure planes dip between 70° and 90°. Along the runout path, particularly well exposed in the northern flow, the channel geometry is concave-up, with high-angle lateral margins and a central surface whose slope angle approximates that of the underlying cone flank; here, slip striations are oriented downslope (Fig. 8e), parallel to the direction of maximum slope, consistent with the 40°–48° dip of the exposed surfaces. In both settings — detachment scars and runout channels — the consistent along-slope orientation of striations supports a translational failure mechanism at the source that evolved into channelized flow downslope.

article in press

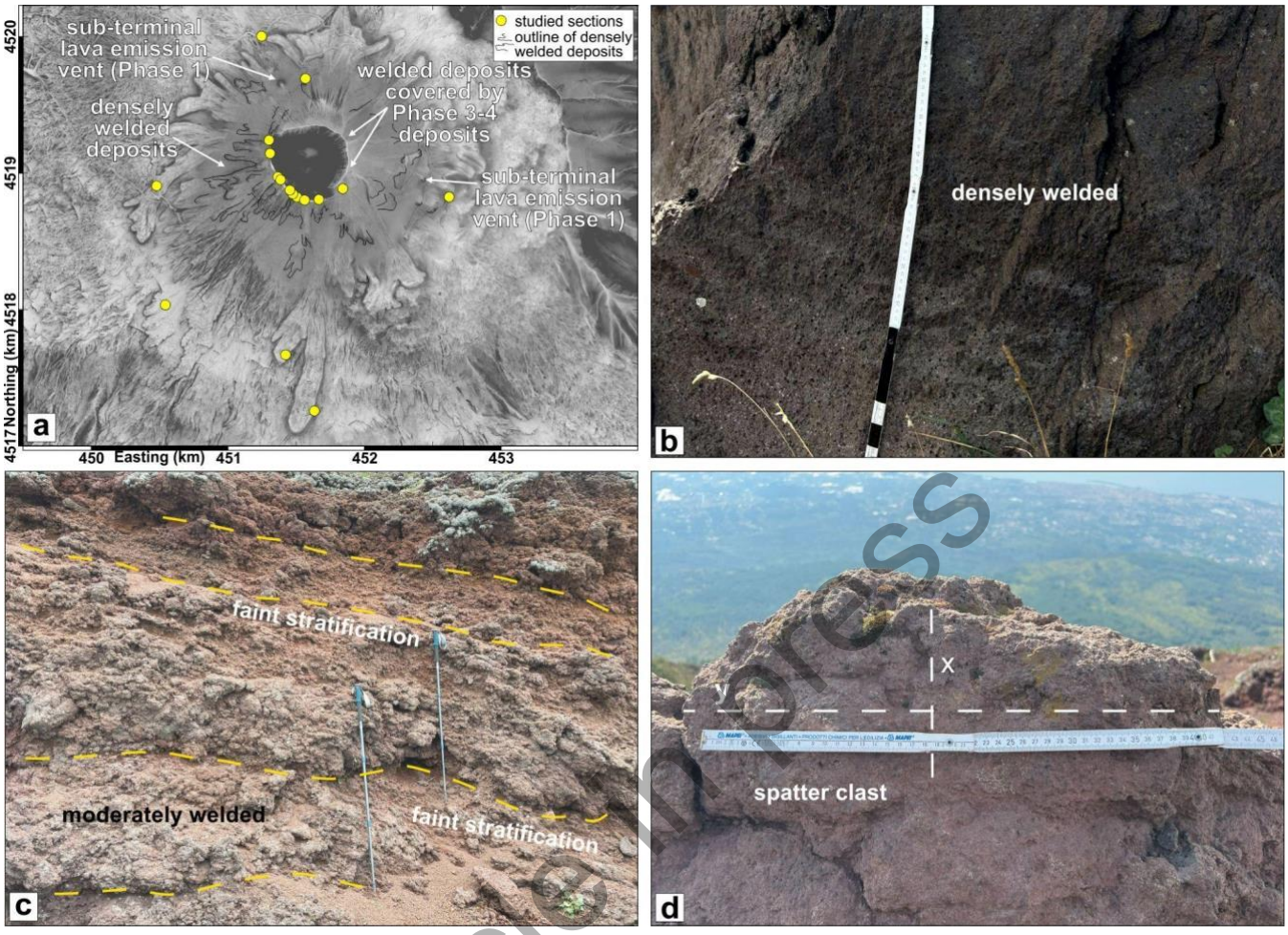

Figure 7: Field and morphostructural features of Phase 2 proximal deposits and dd-PDC detachment surfaces at Vesuvius. (a) Sky-view-factor map showing the location of analysed sections and remnants of densely welded deposits. (b) Field photograph illustrating the densely welded facies. (c) Juxtaposition of distinct moderately welded spatter units; climbing sticks for scale (1.50 m). (d) Geometry of an individual spatter clast.

article in press

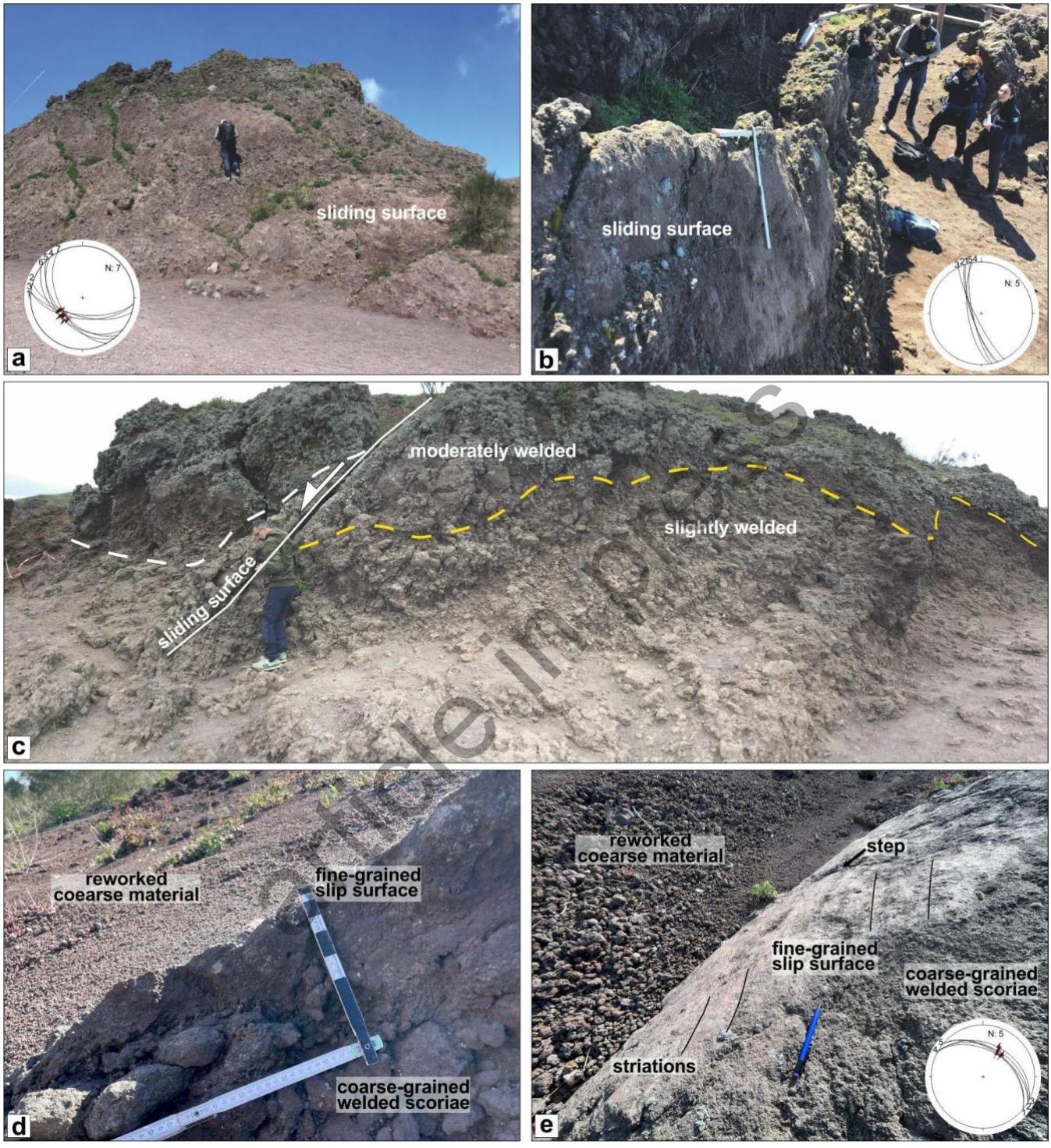

article in press

Figure 8: (a) dd-PDC sliding surface cutting a spatter deposit; inset shows lower-hemisphere equal-area stereographic projection of the sliding plane and associated slip vectors. (b) Close-up of a dd-PDC sliding surface with corresponding

stereographic projection (inset). (c) Juxtaposition of spatter units with contrasting welding intensity; a sliding surface cuts the sequence (yellow dashed line on the right) and is subsequently overlain by a younger spatter layer (white dashed line on the left). d) Field photograph showing a cross-section of a fine-grained, cohesive slip surface. e) Field photograph showing the fine-grained slip surface with a series of kinematic indicators such as orthogonal steps and striations overlying the coarse grained portion of the scoriae deposit. Pen for scale, Lower hemisphere stereographic projection shows the main slip plan orientation and down-dip slip.

Mapping, runout and volume of dd-PDCs

The DEM of Difference (1943 hDSM minus the 2013 LiDAR DTM; Fig. 9a) quantifies elevation changes since the 1944 eruption and forms the basis for estimating the volumes of individual dd-PDC deposits (Table 2). This estimate should be regarded as a minimum, since both the detachment zones and the dd-PDC deposits — whose surface morphology is directly captured by the 2013 LiDAR survey — may have undergone post-eruptive morphological changes induced by erosion in the ~70 years elapsed since the 1944 eruption. The newly formed crater shows elevation decreases exceeding 250 m, whereas the north-eastern sector records elevation increases of up to ~50 m, reflecting material accumulation dominated by Phase 2 deposits. The DoD also allows the radial distance from the 1944 crater rim to be measured, providing first-order estimates of dd-PDC runout and their relationship with pre-existing breaks in slope (Fig. 9a). Most dd-PDCs travelled distances of less than 1 km, although a few extended beyond this threshold. For each suitable dd-PDC we measured the runout length (L) as the incremental distance along the PDC trajectory between the detachment area and the most distal point along the inferred flow path. If curved, this distance is greater than considering the linear distance alone. The eastern sector is characterised by a single dd-PDC deposit with the largest estimated volume (3.05×10^6 m^3; Fig. 9a and Table 2). In contrast, the northern, southern and western sectors experienced multiple collapses. The western sector produced five distinct dd-PDC deposits, each with relatively small individual volumes. Individual collapse events were identified through the combined analysis of mapped detachment scars, associated deposits, historical photographs, field observations and stratigraphic relationships, rather than on the basis of welding degree or individual slip surfaces alone. When plotted in logarithmic space, a clear power-law relationship is observed between detachment-scar area and deposit volume (Fig. 9b), indicating that larger source areas are associated with proportionally larger deposit volumes.

Table 2: Topographic change detection results (Δ_z = 3.74 m)

Flow n.	Area (m^2)	Volume (m^3)	Δ_{Volume} (m^3)
1	3.43×10^4	3.06×10^6	1.28×10^5

article in press

2	1.89×10^5	5.52×10^5	7.07×10^5
3	3.30×10^4	1.56×10^5	1.24×10^5
4	5.73×10^4	1.94×10^5	2.14×10^5
5	3.29×10^5	5.76×10^5	1.23×10^6
6	1.25×10^5	1.07×10^5	4.66×10^5
7	5.50×10^4	9.57×10^5	2.06×10^5
8	1.93×10^5	1.23×10^5	7.23×10^5
9	8.28×10^4	1.64×10^5	3.10×10^5
10	1.06×10^5	3.74×10^5	3.95×10^5
11	3.88×10^4	3.47×10^5	1.45×10^5
12	2.65×10^4	1.09×10^6	9.91×10^4
13	5.39×10^4	6.62×10^4	2.02×10^5
14	7.92×10^4	8.89×10^4	2.96×10^5
15	1.00×10^5	3.83×10^6	3.76×10^5
16	3.14×10^4	8.86×10^4	1.17×10^5

503

504

article in press

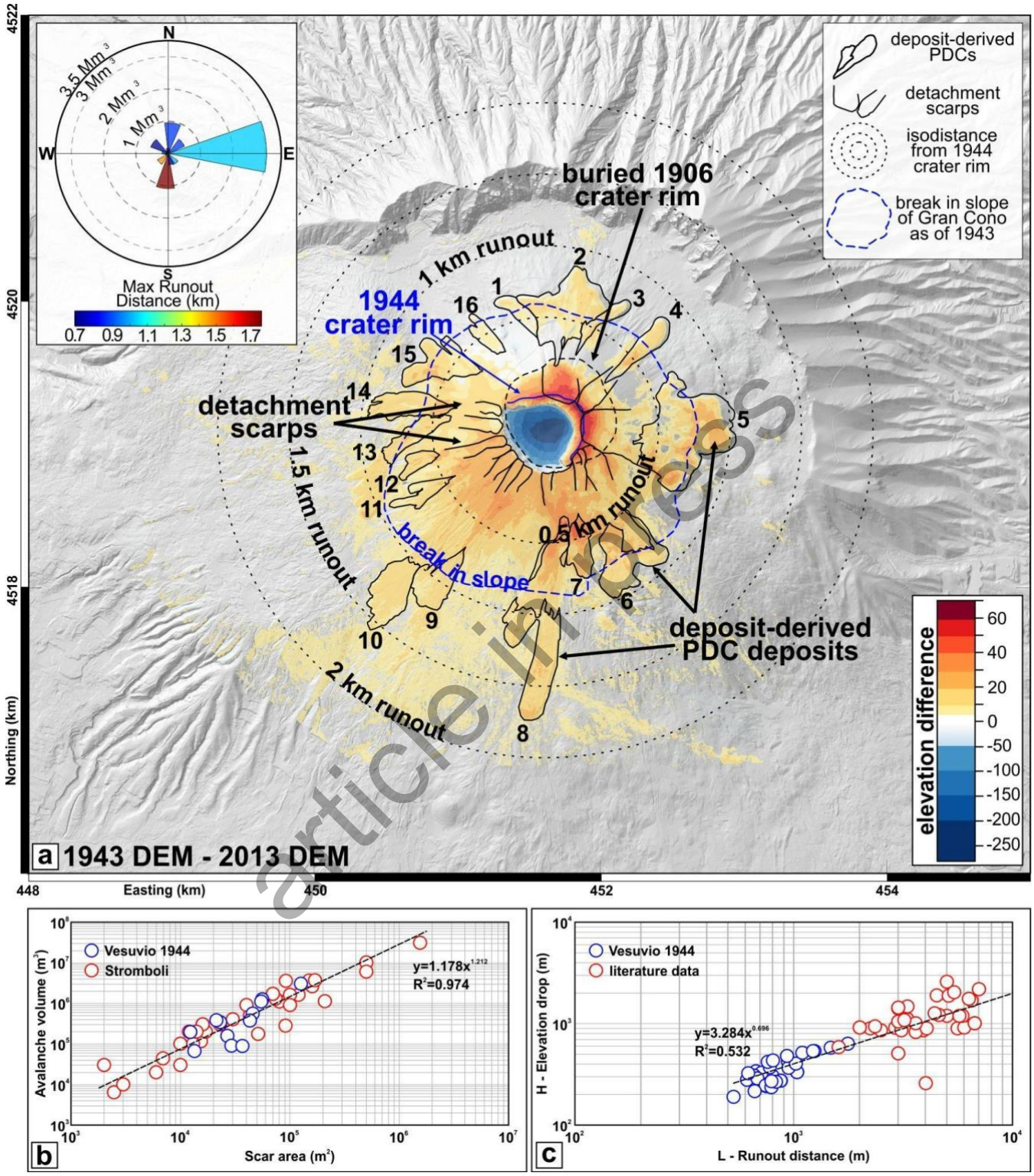

article in press

505

Figure 9: a) Elevation difference (DoD) between the 1943 historical digital surface model (hDSM) and the 2013 LiDAR-derived digital terrain model, illustrating topographic changes associated with the 1944 eruption of Vesuvius. (b) Log–log relationship between dd-PDC volume and corresponding detachment area; the black dashed line indicates a power fit encompassing the available data (data from Casalbore et al., 2010; Di Traglia et al., 2025; this study). (c) Log-Log Relationship between elevation drop (H) and runout distance (L) for individual dd-PDCs (data from Calder et al., 1999); the black dashed line indicates a power fit encompassing the available data.

Discussion

Timing and failure mechanism of the 1944 dd-PDCs

The integration of historical evidence, field relationships and hDSM-based morphometric analysis indicates that gravitational collapse events of deposits emplaced during the lava-fountaining phase (Phase 2) generated dd-PDCs during the 1944 eruption of Vesuvius. No evidence supports the initiation of dd-PDCs during the subsequent mixed-explosive or seismic–explosive phases (as proposed by Hazlett et al., 1991 and Cagnoli et al., 2015), when only small PDCs related to partial column collapse were produced (Imbò, 1949; Cole and Scarpati, 2010). Stratigraphic relationships provide a robust temporal constraint on the timing of failure. Along the northern and eastern flanks, detachment scars systematically truncate Phase 2 fountain-derived deposits and are subsequently infilled and capped by tephra and ash from Phases 3 and 4. Although late-stage fallout does not systematically overlie all dd-PDC deposits, the infilling of collapse cavities by younger pyroclastic material unequivocally constrains failure to Phase 2 (Fig. 2a). This relationship is further confirmed in the southern sector, where Phase 3 fallout directly overlies the Phase2 dd-PDC deposit with the greatest runout, demonstrating that remobilisation occurred prior to the onset of sustained mixed-explosive activity (Fig. 5). Morphological evidence independently supports this interpretation.

The DEM of Difference shows that all detachment scars are located along the outer margin of the lava platform that progressively filled the 1906 crater prior to 1944. No scars are associated with the inner crater walls excavated during the crater-forming events of Phases 3–4. The burial of these scars beneath late-stage fallout further constrains their formation to an early eruptive stage, before major summit reorganisation took place.

Field observations reveal a mechanically stratified proximal succession that strongly conditioned failure. Phase 2 deposits consistently comprise a laterally continuous, densely welded basal spatter unit resting directly on the lava platform, overlain by a heterogeneous alternation of moderately welded, poorly welded spatter and loose lapilli beds. This architecture produces sharp vertical and lateral contrasts in welding intensity, porosity, clast sintering and internal fabric over centimetre- to decimetre-scale intervals. Mapped slip surfaces are systematically localised

article in press

within moderately to poorly welded horizons, where they truncate low-angle spatter stratification and locally display polished surfaces and shear-related grooves. In contrast, densely welded basal units show no evidence of internal shear or detachment, indicating that they acted as mechanically competent foundations during failure.

Topographic and mechanical controls on collapse magnitude

The geometry of the pre-eruptive summit exerted a first-order control on both the magnitude and spatial distribution of collapses. Prior to March 1944, the crater excavated during the 1906 eruption had been completely infilled by lava flows emplaced between 1913 and 1944, forming a broad, relatively flat summit lava platform bounded by steep outer slopes (Fig. 5a). The vent active during Phase 2 was eccentrically located in the south-western sector of this platform, producing an asymmetric pattern of fountain-derived accumulation (Fig. 9). The hDSM and DoD analyses show that the preserved thickest accumulations developed in the northern and eastern sectors, locally exceeding ~60 m above the flat-lying (<10°) pre-existing surface (Fig. 5b). These sectors correspond to the largest dd-PDCs, with volumes up to ~3 Mm^3 and runouts approaching ~1 km from the 1944 crater rim. In contrast, the western and north-western sectors, where Phase 2 deposits were emplaced directly onto the steep (>30°) remnants of the 1906 crater rim (Fig. 5a), experienced multiple small-volume collapses with runouts consistently confined within ~1 km. The southern sector represents an intermediate configuration, where a large dd-PDC achieved the longest runout of the eruption (>1.5 km), facilitated by a more distant break in slope and a steeper, more extended downslope path (Fig. 9). Our volume estimates are broadly consistent with those reported by Hazlett et al. (1991), with most dd-PDCs having volumes $<10^6$ m^3. However, unlike Hazlett et al. (1991), who reported maximum dd-PDC volumes of ~1×10^6 m^3, our reconstruction identifies several events exceeding this threshold, with volumes reaching up to ~3.8×10^6 m^3. Moreover, using field evidence and hDSM and DoD analyses we identified more dd-PDC bodies, especially on the western flank of the Gran Cono (dd-PDC 9-12 in Fig. 9a). Volumetric data, inclusive of similar values from the literature (Calder et al., 1999; Casalbore et al., 2010; Di Traglia et al., 2025), show limited scatter around the best-fit trend, which supports the robustness of the empirical scaling across the analysed events. This relationship highlights a systematic coupling between the extent of the source area and the magnitude of individual dd-PDCs, without implying constant failure thickness. A positive correlation is also observed on a logarithmic scale between the elevation drop from the source to the deposition site and the corresponding runout distance (see Fig. 9c). Although characterised by greater scatter than the area–volume relationship, this trend indicates that greater available relief is generally associated with longer runout distances. This is consistent with the idea that gravitational potential energy has a first-order influence on flow mobility and is reflected by the occurrence of deposition near the break in slope of the underlying surface (Fig. 9a, Sulpizio et al., 2016). The

article in press

569 calculated volume of mapped dd-PDCs range between 10^5-10^6 m^3 with two bigger bodies to the north and east
570 (number 2 and 5 in Fig. 10a). The maximum volume is recorded for the dd-PDC detached on the east (number 5 in
571 Figs. 8a, 9a), which is comparable to Fuego 2018 average flows (Fig. 10b). On the other hand, the average
572 avalanche volume (Fig. 10b) is comparable with the average value at Arenal volcano, and smaller than during
573 Etna's recent paroxysms (Fig. 10b).
574

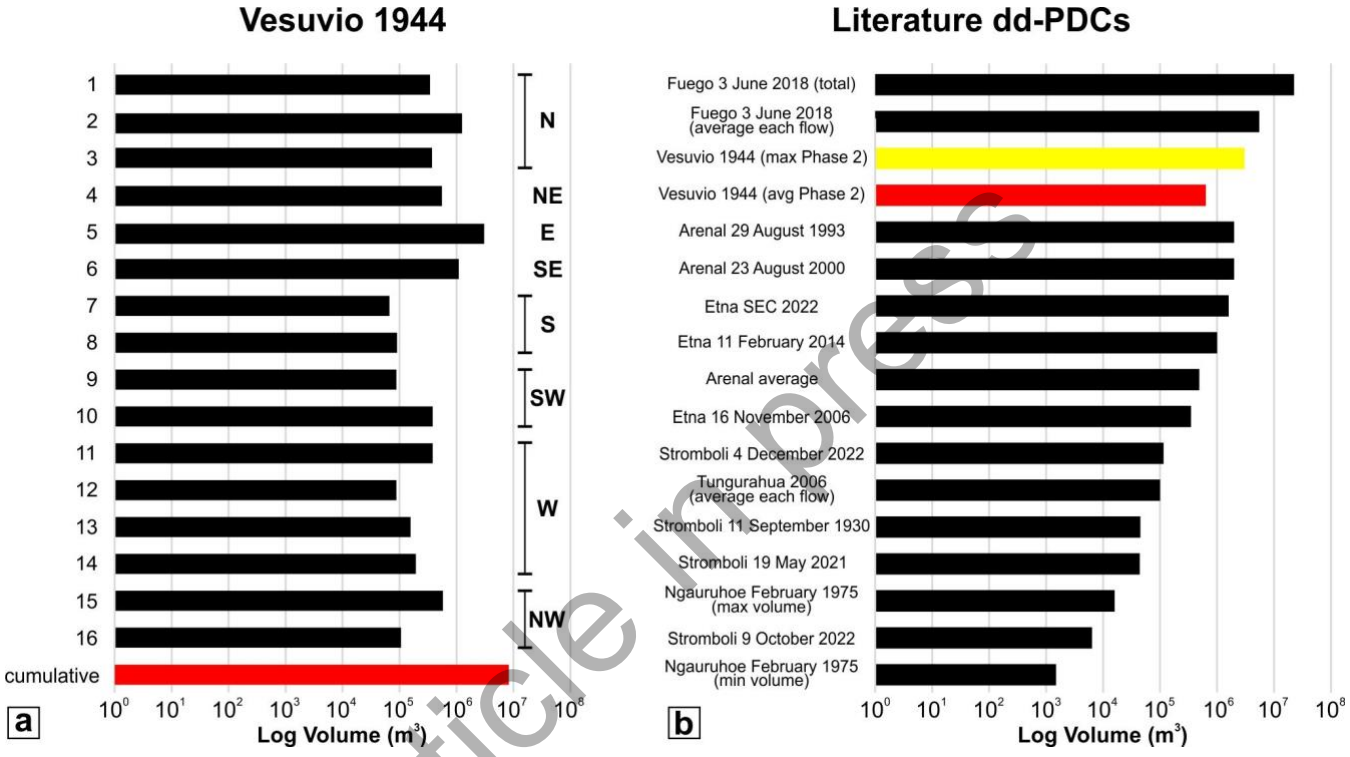

575

576 **Figure 10**: a) Histogram showing the volumes of individual dd-PDCs generated during the 1944 Vesuvius eruption,
577 following the clockwise spatial distribution shown in Figure 9a. (b) Histogram comparing the maximum and average
578 volumes of the 1944 Vesuvius dd-PDCs with values reported in the literature (see Di Traglia et al., 2024, 2026). Note
579 that the Tungurahua volumes reported by Kelfoun et al. (2009) and Bernard et al. (2014, 2016) represent cumulative
580 deposit volumes or assumed input volumes for numerical models, rather than volumes of individual PDC events.
581

582 Together, these observations indicate that dd-PDC generation during the 1944 eruption was governed by rapid
583 proximal accumulation of hot, variably welded fountain-derived material on a geometrically favourable substrate.
584 Failure preferentially involved mechanically weak, incompletely welded horizons and occurred once gravitational
585 stability thresholds were exceeded along the margins of the lava platform. The observed localisation of slip surfaces
586 within moderately to slightly welded horizons further suggests that the mechanical behaviour of the proximal
587 succession cannot be explained solely by either the strength of the rock mass or the presence of stratigraphic

article in press

discontinuities. Rather, the field evidence indicates a mechanically stratified succession in which both the strength of individual volcaniclastic units and the geometry and shear strength of stratigraphic discontinuities jointly control failure initiation and propagation. Recent slope-stability models developed for deposit-derived PDC initiation have shown that considering these two complementary failure mechanisms provides a more realistic representation of instability than adopting either rock-mass strength or discontinuity-controlled failure alone (Di Traglia et al., 2023a,b, 2024, 2026). The preferential occurrence of polished slip surfaces within moderately welded horizons is consistent with this conceptual framework and supports the interpretation that mechanical heterogeneity exerted a first-order control on failure localisation during the 1944 eruption. No exceptional external forcing, such as intense seismic shaking or major crater instability, is required to explain the observed timing, distribution and characteristics of the dd-PDCs (Hazlett et al., 1991; Cagnoli et al., 2015). This mechanism is consistent with a Fuego-type end-member behaviour, in which deposit collapse is primarily controlled by accumulation rate, mechanical heterogeneity and summit geometry, rather than by magma thrust or deep-seated structural failure (Risica et al., 2022; Di Traglia et al., 2026).

Fuego-type versus Arenal-type dd-PDCs at Vesuvius

The failure processes reconstructed for the 1944 eruption of Vesuvius can be framed within a broader context of dd-PDC generation through comparison with other documented cases of crater-rim and proximal deposit instability. In this perspective, the 1944 event represents a clear example of a Fuego-type dd-PDC endmember, in contrast to the multiple (at least two) collapse episodes reported during the 1822 eruption of Vesuvius (Monticelli and Covelli, 1823), which are more consistent with an Arenal-type behaviour. A defining feature of the 1944 sequence is that collapse was triggered by the rapid accumulation of fire-fountain-derived material on a pre-existing substrate characterised by mechanically favourable conditions. Failure occurred once critical thresholds in deposit thickness and slope angle were exceeded along the margins of the lava platform, exploiting internal mechanical heterogeneity rather than requiring additional external forcing. The resulting dd-PDCs were limited in number, spatially concentrated in sectors of maximum accumulation, and strongly influenced by summit morphology in terms of both volume and runout. Such behaviour is characteristic of Fuego-type systems, in which deposit collapse is primarily controlled by accumulation rate, substrate geometry and welding-related contrasts within hot proximal deposits (Risica et al., 2022; Charbonnier et al., 2023; Di Traglia et al., 2026). In contrast, the dd-PDCs generated during the 1822 eruption exhibit a markedly different pattern. That eruption was characterised by multiple collapse events affecting the crater rim during phases of lava effusion, producing repeated remobilisation of hot material rather than a limited number of failures following sustained accumulation (Monticelli and Covelli, 1823). In such

article in press

cases, collapse reflects progressive destabilisation of the rim driven by shallow magmatic forcing. This behaviour aligns with the Arenal-type endmember, where dd-PDCs are generated by repeated rim failures associated with effusion and overflow, and where the distinction between accumulation-driven and structurally driven collapse becomes less sharp. The contrast between these two behaviours highlights that dd-PDCs do not represent a single process continuum but instead arise from distinct mechanical pathways. In Fuego-type systems, such as the 1944 eruption, the key control is the development of a mechanically stratified proximal blanket, requiring accumulation prior to failure occurrence. Once instability is reached, collapse is abrupt and strongly modulated by pre-eruptive topography. In Arenal-type systems, such as the 1822 eruption, instability develops incrementally through repeated effusive episodes, producing (multiple) smaller collapses over time.

Scaling relationships and failure geometry

The empirical area–volume relationship derived in this study (exponent b=1.212 in Fig 9) indicates that landslide volume increases more rapidly than area, implying that mean failure thickness is not constant but increases only moderately with landslide size. Such behaviour departs from the end-member case of planar sliding characterised by nearly constant thickness (b≈1) (Malamud et al., 2004; Guzzetti et al., 2009), while remaining markedly different from the scaling expected for deep-seated rotational slides, for which depth scales proportionally with landslide length and geometrically constrained volume estimates imply an implicit exponent close to b≈1.5 (e.g. Skempton and Hutchinson, 1969; Catani et al., 2005). The intermediate scaling behaviour observed here is consistent with process-based interpretations derived from previous slope stability modelling of proximal volcaniclastic deposits, which indicate that failure initiation and propagation are governed by the combined effects of mechanical stratification and bulk rock-mass strength (Di Traglia et al., 2023a,b, 2024; 2026). In this framework, failure develops through a composite mechanism that is neither purely structure-controlled nor purely rock-mass–controlled, with rupture surfaces progressively involving multiple stratigraphic levels without evolving into fully rotational geometries (Di Traglia et al., 2023a,b, 2024; 2026). Accordingly, the observed scaling exponent can be interpreted as reflecting a physically meaningful intermediate regime, consistent with stratigraphy- and material-controlled instabilities leading to dd-PDC generation from steep proximal slopes. Similar power-law formulations of area–volume relationships are widely documented in landslide inventories, although with exponents varying as a function of landslide type and failure geometry (Malamud et al., 2004; Guzzetti et al., 2009).

Controls on dd-PDC mobility

article in press

649 The mobility of dd-PDCs generated during the 1944 eruption of Vesuvius reflects the combined influence of source
650 geometry, source volume, slope configuration and the physical properties of the remobilised deposits.
651 Morphometric analysis shows that most dd-PDCs travelled less than ~1 km from their detachment areas, with only
652 a few exceeding this distance and the longest runout reaching slightly more than 1.5 km. These values fall within
653 the range expected for dense granular flows generated by the gravitational failure of hot volcaniclastic material and
654 are markedly lower than those commonly reported for highly mobile column-collapse PDCs or dilute surges
655 (Hayashi and Self, 1992; Calder et al., 1999). The systematic termination of the deposits near breaks in slope,
656 together with the strong correlation between local topography and runout distance, indicates that flow mobility was
657 primarily controlled by the underlying morphology of the volcanic cone.
658 Relationships between elevation drop (H) and runout distance (L) display a broadly linear trend (Fig. 9c), indicating
659 that gravitational potential exerted a first-order control on flow mobility. Likewise, the positive correlation between
660 detachment-scar area and deposit volume suggests that the magnitude of individual dd-PDCs was primarily
661 governed by the size of the failed source area. The largest volumes and longest runouts are associated with thick
662 Phase 2 accumulations emplaced on the broad summit lava platform and subsequently remobilised from its outer
663 margins, allowing the flows to access longer and steeper downslope trajectories. In contrast, smaller-volume dd-
664 PDCs initiated directly on the steep crater-rim slopes travelled considerably shorter distances despite comparable
665 emplacement temperatures, highlighting the importance of slope length, slope inclination and the position of the
666 break in slope in controlling flow propagation. Together, these observations are consistent with translational slope
667 failures followed by downslope transport as dense granular flows, in agreement with classical descriptions of
668 granular avalanches and dense pyroclastic flows (Hayashi and Self, 1992; Calder et al., 1999).
669 The source material consisted predominantly of hot spatter- and lapilli-rich deposits characterised by limited fine-
670 ash content, high permeability and variable, generally incomplete welding (Cole and Scarpati, 2010). During
671 transport, progressive comminution of juvenile clasts would have continuously generated fine ash, as demonstrated
672 experimentally for pumice-rich granular flows (Figueiredo et al., 2025). Such fragmentation may have promoted
673 transient fragmentation-induced fluidisation (Breard et al., 2023), temporarily reducing effective friction during the
674 earliest stages of transport. Nevertheless, the relatively short runout distances, the marked topographic control on
675 deposition, and the systematic accumulation of deposits close to breaks in slope indicate that any fluidisation effects
676 were probably short-lived and that frictional resistance remained the dominant control on overall flow mobility
677 throughout emplacement.
678 Figure 11 summarises the proposed conceptual model for dd-PDC generation during the 1944 eruption. The pre-
679 eruptive summit configuration (Fig. 11a), characterised by a broad lava platform bounded by steep outer slopes,

article in press

exerted a primary control on collapse initiation. Small-volume failures originated directly from the steep crater flanks during the early stages of Phase 2 (Fig. 11b), whereas continued accumulation of variably welded fountain-fed deposits on the lava platform progressively increased the load until larger collapses were triggered along its outer margins (Fig. 11c). This sequence produced the present-day two-fold stratigraphic architecture of the Gran Cono, where the north-eastern sector preserves the complete eruptive succession, while other sectors expose only the lower part of the Phase 2 succession owing to subsequent collapse and burial (Fig. 11d).

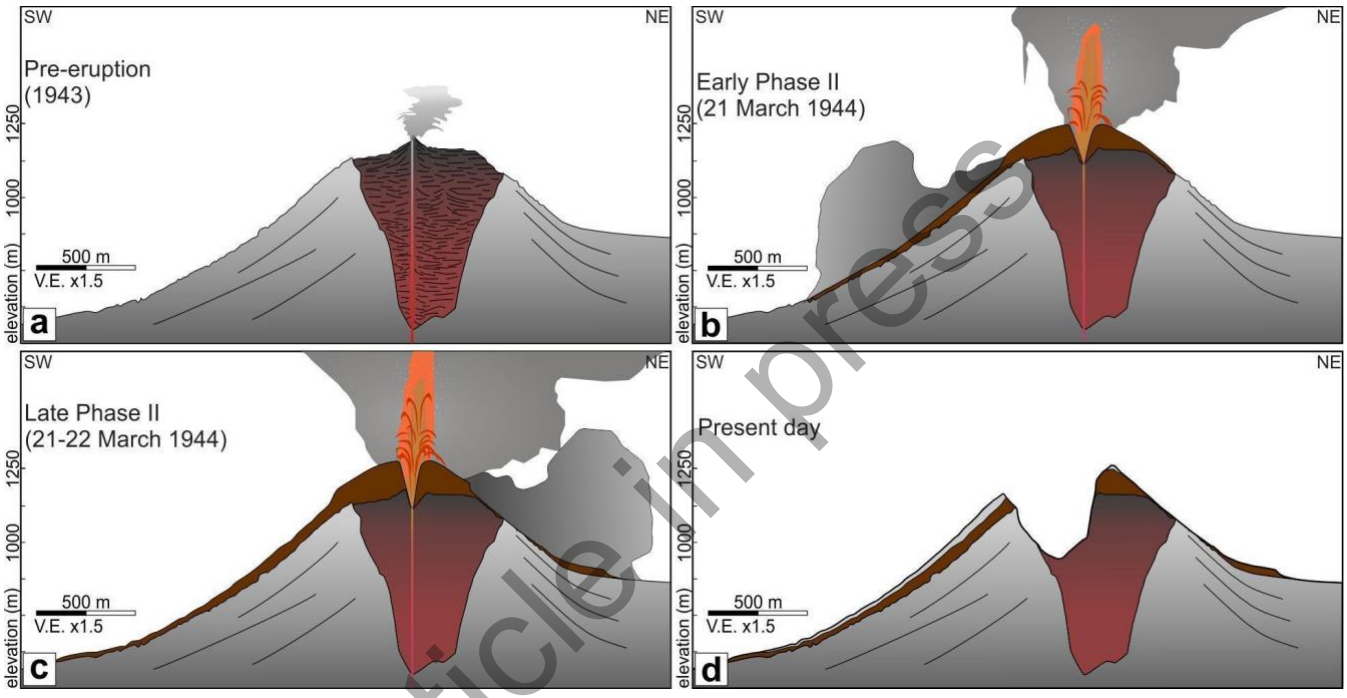

Figure 11. Simplified sketch showing a NE-SW oriented cross section through the crater area. a) Pre-eruptive configuration showing the lava platform infilling the 1906 crater, constructed based on data from Malladra (1914); b) Early Phase 2 of the eruption with small dd-PDC detaching from the outer flank; c) Late Phase 2 of the eruption with large dd-PDC detaching from high-accumulation of variably welded material on the former lava platform; d) Present-day morphological configuration with eruptive material from Phases 3-4 overlying the dd-PDC deposits. Abbreviations: V.E. vertical exaggeration.

Conclusions

This study provides a comprehensive reassessment of dd-PDCs generated during the 1944 eruption of Vesuvius by integrating historical chronicles, field-based stratigraphic observations and high-resolution morphometric analyses derived from historical and modern digital elevation models. This multi-source approach allows the mechanisms,

Article in press

timing and mobility of the 1944 dd-PDCs to be constrained with a level of detail not previously achieved for this eruption. Our results show that all dd-PDCs generated in 1944 originated from gravitational collapse of hot, fountain-derived deposits emplaced during the lava-fountaining phase (Phase 2). Failure was controlled by rapid proximal accumulation of variably welded spatter and lapilli on a geometrically favourable substrate and preferentially exploited mechanically weak, incompletely welded horizons within the deposit pile. Instability developed once critical gravitational thresholds were exceeded along the margins of the pre-existing lava platform, consistent with a Fuego-type end-member behaviour.

The Vesuvius record further demonstrates that a single volcanic edifice can alternate between distinct dd-PDC generation mechanisms depending on eruptive style and summit configuration. The contrast between the Arenal-type behaviour (magma-induced failure; Di Traglia et al. 2026) inferred for the 1822 eruption and the Fuego-type behaviour (gravity-induced failure; Di Traglia et al. 2026) documented for 1944 reflects fundamental differences in proximal deposition processes and inherited summit morphology. In 1944, the presence of a broad lava platform promoted thick, laterally extensive accumulation during lava fountaining, whereas in 1822 collapse occurred directly along a steep crater rim without the mediation of a platform-like surface. This distinction highlights the critical role of morphological inheritance and accumulation patterns in governing dd-PDC generation. Analysis of flow mobility indicates that the 1944 dd-PDCs propagated as dense granular flows, with runout distances and scaling relationships primarily controlled by source volume, elevation drop and topographic configuration. The Vesuvius case shows that significant dd-PDC hazard can arise under conditions of rapid proximal accumulation and favourable geometry alone. These findings have important implications for volcanic hazard assessment. They demonstrate that dd-PDCs may be generated during eruptive phases commonly perceived as low to moderate in intensity, such as sustained lava fountaining, and that hazard levels cannot be inferred from eruptive intensity alone. Identifying periods of enhanced dd-PDC susceptibility therefore requires explicit consideration of summit morphology, accumulation rates and the internal mechanical structure of proximal deposits. More broadly, the framework developed here provides a transferable basis for interpreting dd-PDC hazards at persistently active volcanoes worldwide, including those with long historical records and limited instrumental monitoring.

article in press

Supplementary material

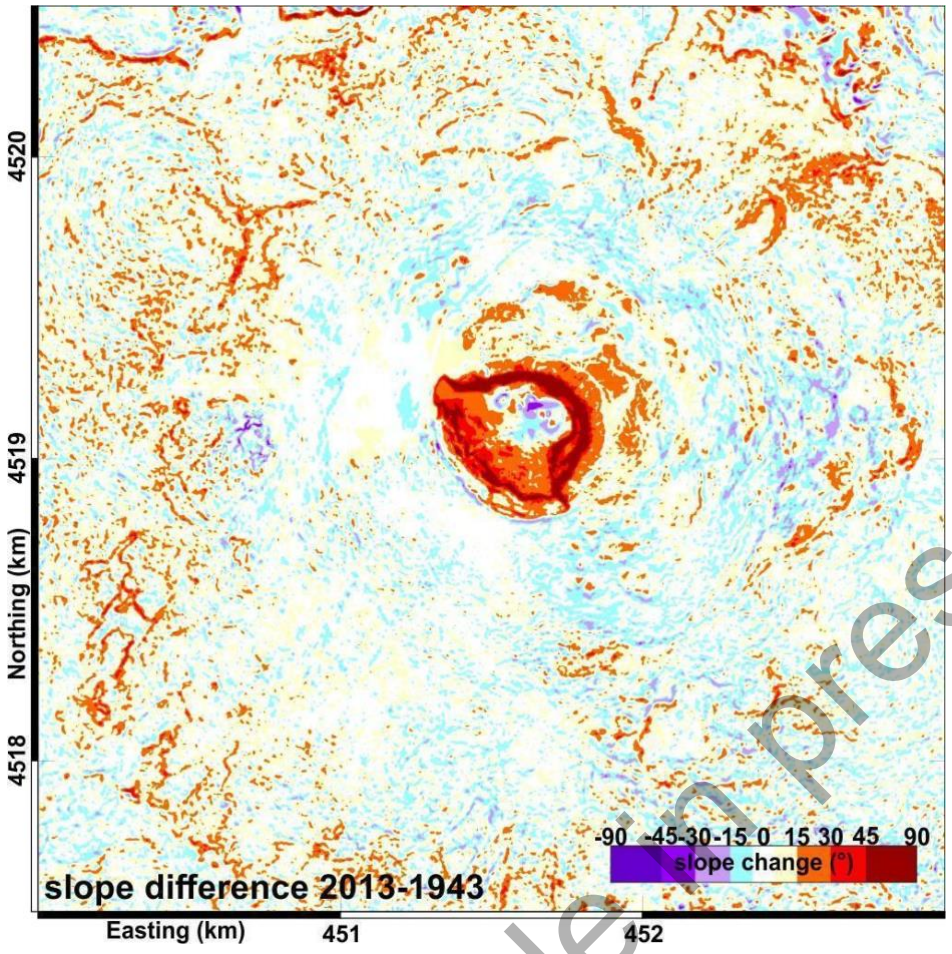

Supplementary Figure 1. Differential slope map between 2013 and 1943 DEMs.

Author contributions

J.N. conducted fieldwork, performed DEM reconstruction and analysis, made the figures and contributed to writing and editing. A.F. contributed to fieldwork, writing and editing. T.O.G., A.B., G.B., A.Fr., R.N. and L.P. contributed to fieldwork and editing. M.F. and A.Fo. contributed to DEM analysis and editing. G.G. contributed to the conceptualisation of the study and editing. E.I. contributed to fieldwork, editing and funding acquisition. A.V. contributed to the conceptualisation of the study, editing and funding acquisition. F.D.T. conceived the study, carried out fieldwork and DEM analysis, led the writing process, contributed to editing, and acquired funding.

Acknowledgements

article in press

We would like to express our sincere gratitude to the Editorial Board of *Volcanica* for their continuous commitment to maintaining a high-quality, community-driven journal. Their dedication represents a valuable service to the volcanological community as a whole. We are especially grateful to our Handling Editor, Rebecca Williams, for her careful guidance throughout the review process, and to the three reviewers—Anke Zernack, Ulrich Küppers and an anonymous reviewer—for the time, expertise and constructive comments they devoted to improving this manuscript. Their thoughtful reviews not only strengthened the quality of our work but also exemplify the essential contribution of reviewers, whose voluntary efforts are fundamental to maintaining rigorous peer review and whose commitment is increasingly vital in ensuring the sustainability of scientific publishing. J.N. would like to thank Dr. P. Allocca for his valuable support in the identification of Ground Control Points (GCPs) in the Vesuvius area. This research has benefited from European Union – Next Generation EU, National Recovery and Resilience Plan Mission 4 - Component 2. Project title: "Causes and consequences of deposit-derived pyroclastic density currents" (P20222BP7J)" [PI: F. Di Traglia; RU Leaders: E. Intrieri (UNIFI); A. Vona (UNIROMA3)]. F. Di Traglia gratefully acknowledges S. Tulino for her administrative support throughout the management of the project.

Data availability

The DoD and the boundaries of the dd-PDC deposits and detachment scars generated in this study are available from the repository at https://www.pi.ingv.it/banche-dati/dod_1943-2013_vesuvio/ and are distributed under the CC BY 4.0 licence. The Istituto Geografico Militare (IGM) is kindly acknowledged for authorising the use of the IGM dataset. The data used in this study were made available free of charge to the authors under an agreement between the Istituto Geografico Militare (IGM) and the Istituto Nazionale di Geofisica e Vulcanologia (INGV) (Authorisation No. 7270, 17 February 2026). Researchers wishing to obtain the IGM dataset should submit a request directly to the IGM. In accordance with the Italian Cultural Heritage and Landscape Code (Legislative Decree No. 42/2004), authorisation for personal, educational, or research purposes carried out on a non-profit basis may be granted free of charge. The 2013 DEM used in this study is publicly available from the Città Metropolitana di Napoli Spatial Information System (SIT) download portal: https://sit.cittametropolitana.na.it/downloads.php.

References

Abbruzzese, D. (1936). Sulla catastrofica esplosione dello Stromboli dell'11 settembre del 1930. Atti Accad. Gioenia Sc. Nat. Catania, 1, 1-33.

article in press

Albino, F., et al. (2020) Using TanDEM-X to measure pyroclastic flow source location, thickness & volume: Application to the 3rd June 2018 eruption of Fuego volcano, Guatemala. J. Volcanol. Geotherm. Res. 406:107063. https://doi.org/10.1016/j.jvolgeores.2020.107063

Alvarado, G.E., et al. (2023) Review of bomb & ash flows: Genesis & case studies of a subset of block & ash flow deposits. Andean Geology 50(3):346-371. https://doi.org/10.5027/andgeoV50n3-3653

Alvarado, G. E., Soto, G. J. (2002) Pyroclastic flow generated by crater-wall collapse & outpouring of the lava pool of Arenal Volcano, Costa Rica. Bull. Volcanol. 63:557–568. https://doi.org/10.1007/s00445-001-0179-9

Andronico, D. et al. (2018) Pyroclastic density currents at Etna volcano, Italy: The 11 February 2014 case study. J. Volcanol. Geotherm. Res. 357:92–105. https://doi.org/10.1016/j.jvolgeores.2018.04.012

Arrighi, S., et al. (2001) Violent strombolian & subplinian eruptions at Vesuvius during post-1631 activity. Bull. Volcanol. 63:126-150. https://doi.org/10.1007/s004450100130

Arzilli, F., La Spina, G., Bamber, E.C., Morgavi, D., Fedele, L., Mancini, L., Prašek, M., Santangelo, I., Chiominto, G., Perrotta, A., Lemaire, T., Balcone-Boissard, H., Giordano, D., Scarpati, C., 2026. The role of crystal-bubble interactions, outgassing and magma composition in the ascent dynamics of alkaline magmas: Implications for eruptions at Vesuvius. Earth and Planetary Science Letters 675, 119771. https://doi.org/10.1016/j.epsl.2025.119771

Báez, W., et al (2024) Complex facies architecture of unusual pyroclastic density current deposits at the Rincón de la Vieja Volcano, Costa Rica. J. Volcanol. Geotherm. Res. 447:108030. https://doi.org/10.1016/j.jvolgeores.2024.108030

Behncke, B., et al. (2008) Pyroclastic density currents resulting from the interaction of basaltic magma with hydrothermally altered rock: an example from the 2006 summit eruptions of Mount Etna, Italy. Bull. Volcanol. 70:1249–1268. https://doi.org/10.1007/s00445-008-0200-7

Bernard, J., et al. (2014) Pyroclastic flow erosion & bulking processes: comparing field-based vs. modeling results at Tungurahua volcano, Ecuador. Bull. Volcanol. 76:1-16. https://doi.org/10.1007/s00445-014-0858-y

Bertagnini, A., et al. (1991). The 1906 eruption of Vesuvius: from magmatic to phreatomagmatic activity through the flashing of a shallow depth hydrothermal system. Bulletin of Volcanology, 53(7):517-532. https://doi.org/10.1007/BF00298153

Bevilacqua, A., et al. (2026) "Assessing deposit-derived pyroclastic flow hazard at Stromboli (Italy): 2. Probabilistic invasion maps." Journal of Geophysical Research: Solid Earth 131.5: https://doi.org/10.1029/2025JB032571.

article in press

Bisson, M., Tadini, A., Gianardi, R., & Angioletti, A. (2021). The use of historical cartography and ALS technology to map the geomorphological changes of volcanic areas: A case study from Gran Cono of Somma-Vesuvius volcano. Geomorphology, 380:107624. https://doi.org/10.1016/j.geomorph.2021.107624

Branney, M. J., & Kokelaar, B. P. (2002). Pyroclastic density currents & the sedimentation of ignimbrites. Geol. Soc. Lond. Mem. 27:1–143. https://doi.org/10.1144/GSL.MEM.2003.027

Breard, E. C., Dufek, J., & Lube, G. (2018). Enhanced mobility in concentrated pyroclastic density currents: An examination of a self-fluidization mechanism. *Geophysical Research Letters*, *45*(2), 654-664.

Breard, E. C., Dufek, J., Charbonnier, S., Gueugneau, V., Giachetti, T., & Walsh, B. (2023). The fragmentation-induced fluidisation of pyroclastic density currents. Nature communications, 14(1), 2079. https://doi.org/10.1038/s41467-023-37867-1

Calder, E. S., et al. (1999). Mobility of pyroclastic flows and surges at the Soufriere Hills Volcano, Montserrat. Geophysical Research Letters, 26(5):537-540. https://doi.org/10.1029/1999GL900051

E. S. Calder, R. Luckett, R. S. J. Sparks, B. Voight, 2002. "Mechanisms of lava dome instability and generation of rockfalls and pyroclastic flows at Soufrière Hills Volcano, Montserrat", The Eruption of Soufrière Hills Volcano, Montserrat from 1995 to 1999, T. H. Druitt, B. P. Kokelaar https://doi.org/10.1144/GSL.MEM.2002.021.01.08

Calvari, S., & Pinkerton, H. (2002) Instabilities in the summit region of Mount Etna during the 1999 eruption. Bull. Volcanol. 63:526-35. https://doi.org/10.1007/s004450100171

Calvari, S., et al. (2016). Monitoring crater-wall collapse at active volcanoes: A study of the 12 January 2013 event at Stromboli. Bull. Volcanol. 78:1-16. https://doi.org/10.1007/s00445-016-1033-4

Calvari, S., et al. (2020) Overflows & pyroclastic density currents in March-April 2020 at Stromboli volcano detected by remote sensing & seismic monitoring data. Remote Sensing 12(18):3010. https://doi.org/10.3390/rs12183010

Carey, R.J., et al. (2008). Contrasting styles of welding observed in the proximal Askja 1875 eruption deposits I: Regional welding. J. Volcanol. Geotherm. Res. 171:1–19. https://doi.org/10.1016/j.jvolgeores.2007.11.020

Casalbore, D., et al. (2022). Integration of remote sensing and offshore geophysical data for monitoring the short-term morphological evolution of an active volcanic flank: a case study from Stromboli Island. Remote Sensing, 14(18):4605. https://doi.org/10.3390/rs14184605

Casalbore, D., et al. (2025). Very fast canyon formation and evolution along active volcanic flanks: A case from Stromboli Island. Geomorphology, 109961. https://doi.org/10.1016/j.geomorph.2025.109961

Catani, F., et al. (2005). Landslide hazard and risk mapping at catchment scale in the Arno River basin. Landslides, 2(4):329-342. https://doi.org/10.1007/s10346-005-0021-0

article in press

Charbonnier, S. J., et al. (2023) Unravelling the dynamics & hazards of the June 3rd, 2018, pyroclastic density currents at Fuego volcano (Guatemala). J. Volcanol. Geotherm. Res. 436:107791. https://doi.org/10.1016/j.jvolgeores.2023.107791

Chester, D., et al. (2015). Human responses to the 1906 eruption of Vesuvius, southern Italy. Journal of Volcanology and Geothermal Research, 296, 1-18. https://doi.org/10.1016/j.jvolgeores.2015.03.004

Cioni, R., et al. (2008). Explosive activity and eruption scenarios at Somma-Vesuvius (Italy): towards a new classification scheme. Journal of Volcanology and Geothermal Research, 178(3), 331-346. https://doi.org/10.1016/j.jvolgeores.2008.04.024

Civico, R., et al. (2024). High-resolution topography reveals morphological changes of Stromboli volcano following the July 2024 eruption. Scientific Data, 11(1), 1219. https://doi.org/10.1038/s41597-024-04098-y

Cole, P. D., et al. (2005) Explosive activity & generation mechanisms of pyroclastic flows at Arenal volcano, Costa Rica between 1987 & 2001. Bull. Volcanol. 67:695–716. https://doi.org/10.1007/s00445-004-0402-6

Cole, P. D.,and Scarpati, C. (2010) The 1944 eruption of Vesuvius, Italy: combining contemporary accounts & field studies for a new volcanological reconstruction. Geological Magazine 147(3):391-415. https://doi.org/10.1017/S0016756809990495

Corna, Lucas, et al. "Field characterization and numerical modelling of a new historical deposit-derived pyroclastic density current at Punta Labronzo, Stromboli, Italy." Bulletin of Volcanology 88.6 (2026): 65.https://doi.org/10.1007/s00445-026-01988-4

Costa, G., & Viccaro, M. (2026). Pyroclastic density currents at mafic volcanic systems: insights from four decades of observations at Mount Etna volcano, Southern Italy. Earth-Science Reviews, 105460. https://doi.org/10.1016/j.earscirev.2026.105460

Cubellis, E., et al. (2016). The last Vesuvius eruption in March 1944: reconstruction of the eruptive dynamic and its impact on the environment and people through witness reports and volcanological evidence. Natural Hazards, 82(1), 95-121. https://doi.org/10.1007/s11069-016-2182-7

Davies, D.K., et al. (1978) Glowing avalanches from the 1974 eruption of the volcano Fuego, Guatemala. Geol Soc Am Bull 89(3):369-384. https://doi.org/10.1130/0016-7606(1978)89<369:GAFTEO>2.0.CO;2

Di Roberto, A., et al. (2014) Pyroclastic density currents at Stromboli volcano (Aeolian Islands, Italy): a case study of the 1930 eruption. Bull. Volcanol. 76:1–14. https://doi.org/10.1007/s00445-014-0827-5

Di Traglia, F., Calvari, S., D'Auria, L., Nolesini, T., Bonaccorso, A., Fornaciai, A., Esposito, A., & Casagli, N. (2018). The 2014 effusive eruption at Stromboli: New insights from in situ and remote-sensing measurements. Remote Sensing, 10(12), 2035. https://doi.org/10.3390/rs10122035

article in press

Di Traglia, F., Fornaciai, A., Favalli, M., Nolesini, T., & Casagli, N. (2020). Catching geomorphological response to volcanic activity on steep slope volcanoes using multi-platform remote sensing. Remote Sensing, 12(3), 438. https://doi.org/10.3390/rs12030438

Di Traglia, F., Fornaciai, A., Casalbore, D., Favalli, M., Manzella, I., Romagnoli, C., Chiocci, F.L., Cole, P., Nolesini, T., & Casagli, N. (2022). Subaerial-submarine morphological changes at Stromboli volcano (Italy) induced by the 2019–2020 eruptive activity. Geomorphology, 400, 108093. https://doi.org/10.1016/j.geomorph.2021.108093

Di Traglia, F., et al. (2023a) Crater-rim collapse at Stromboli volcano: understanding the mechanisms leading from the failure of hot rocks to the development of glowing avalanches. Nat. Haz. 115(3):2051-2068. https://doi.org/10.1007/s11069-022-05626-y

Di Traglia, F., et al. (2024) Generation of deposit-derived pyroclastic density currents by repeated crater rim failures at Stromboli Volcano (Italy). Bull Volcanol 8(8):69. https://doi.org/10.1007/s00445-024-01761-5 .

Di Traglia, F., et al. (2025) Operational radar monitoring of crater rim failure at Stromboli volcano (Italy). Nat Hazards 121(15):18391-409. https://doi.org/10.1007/s11069-025-07521-8

Di Traglia, F., et al. (2026). Explaining the origin of deposit-derived pyroclastic density currents. Bulletin of Volcanology, 88(3), 26. https://doi.org/10.1007/s00445-026-01948-y

Dualeh, E. W., et al. (2021) Analyzing explosive volcanic deposits from satellite-based radar backscatter, Volcán de Fuego, 2018. J. Geophys. Res. Solid Earth 126:e2021JB022250. https://doi.org/10.1029/2021JB022250

Falasconi, A., et al. (2025). Long-term precursors to large explosive eruptions of Vesuvius: evidence from the opening phase of the Avellino Plinian eruption. Bulletin of Volcanology, 87(3), 22. https://doi.org/10.1007/s00445-025-01808-1

Figueiredo, C., Kueppers, U., Pereira, L., Depauli, L., Esenyel, S., & Dingwell, D. B. (2025). Shape evolution of pumice during granular flow. Communications Earth & Environment, 6(1), 941. https://doi.org/10.1038/s43247-025-02936-4

Fornaciai, A., Behncke, B., Favalli, M., Neri, M., Tarquini, S., & Boschi, E. (2010). Detecting short-term evolution of Etnean scoria cones: a LIDAR-based approach. Bulletin of Volcanology, 72(10), 1209-1222. https://doi.org/10.1007/s00445-010-0394-3

Fulignati, P., et al. (2004). Towards a reconstruction of the magmatic feeding system of the 1944 eruption of Mt Vesuvius. Journal of Volcanology and Geothermal Research, 133(1-4), 13-22. https://doi.org/10.1016/S0377-0273(03)00388-3

article in press

Giordano, G., & De Astis, G. (2021) The summer 2019 basaltic Vulcanian eruptions (paroxysms) of Stromboli. Bull. Volcanol. 83:1-27. https://doi.org/10.1007/s00445-020-01423-2

Giordano, G., Cas, R., & Wright, J. V. (2024). Subaerial Pyroclastic Density Currents (Pyroclastic Flows and Surges) Origins, Types, and Deposit Characteristics. In Volcanology: Processes, Deposits, Geology and Resources (pp. 693-889). Cham: Springer International Publishing. https://doi.org/10.1007/978-3-319-66613-6_10

Guzzetti, F., et al. (2009). Landslide volumes and landslide mobilization rates in Umbria, central Italy. Earth and Planetary Science Letters, 279(3-4), 222-229. https://doi.org/10.1016/j.epsl.2009.01.005

Harnett, C. E., & Heap, M. J. (2021). Mechanical and topographic factors influencing lava dome growth and collapse. Journal of Volcanology and Geothermal Research, 420, 107398. https://doi.org/10.1016/j.jvolgeores.2021.107398

Hazlett, R. W., et al. (1991). Geology, failure conditions, and implications of seismogenic avalanches of the 1944 eruption at Vesuvius, Italy. Journal of Volcanology and Geothermal Research, 47(3-4), 249-264. https://doi.org/10.1016/0377-0273(91)90004-J

Hayashi, J. N., & Self, S. (1992). A comparison of pyroclastic flow and debris avalanche mobility. Journal of Geophysical Research: Solid Earth, 97(B6), 9063-9071. https://doi.org/10.1029/92JB00173

Imbò, G. (1928) Parossismo di Stromboli nel settembre 1930. Bull. Volcanol. 5(1):177-185. https://doi.org/10.1007/BF02718563

Imbò, G. (1949) L'attività eruttiva vesuviana e relative osservazioni nel corso dell'intervallo eruttivo 1906-1944 ed in particolare del parossismo del marzo 1944. Annali dell'Osservatorio Vesuviano, V Serie, Vol. unico.

James, M.R., Robson, S., (2012). Straightforward reconstruction of 3D surfaces and topography with a camera: accuracy and geoscience application. J. Geophys. Res. Earth 117 (F3). https://doi.org/10.1029/2011JF002289

Kelfoun, K., et al. (2009) Testing the suitability of frictional behaviour for pyroclastic flow simulation by comparison with a well-constrained eruption at Tungurahua volcano (Ecuador). Bull. Volcanol. 71:1057-1075. https://doi.org/10.1007/s00445-009-0286-6

Lacroix A (1906) Sur l'eruption du Vesuve et en particulier sur le phenomenes explosifs. C R Ac Sci 23 Avril 1906, 941

Lazzari A., (1947). Segnalazione della caduta in Albania delle ceneri del Vesuvio dell'eruzione del Marzo 1944. Bollettino Società dei Naturalisti di Napoli 57, 3–6.

Lerner, G. A., et al. (2022) The hazards of unconfined pyroclastic density currents: A new synthesis & classification according to their deposits, dynamics, & thermal & impact characteristics. J. Volcanol. Geotherm. Res. 421:107429. https://doi.org/10.1016/j.jvolgeores.2021.107429

article in press

Lube, G. et al. (2007) Flow & deposition of pyroclastic granular flows: A type example from the 1975 Ngauruhoe eruption, New Zealand. J. Volcanol. Geotherm. Res. 161:165–186. https://doi.org/10.1016/j.jvolgeores.2006.12.003

Lube, G., Breard, E. C., Esposti-Ongaro, T., Dufek, J., & Brand, B. (2020). Multiphase flow behaviour and hazard prediction of pyroclastic density currents. *Nature Reviews Earth & Environment*, *1*(7), 348-365. https://doi.org/10.1038/s43017-020-0064-8

Malamud, B. D., et al. (2004). Landslide inventories and their statistical properties. Earth Surface Processes and Landforms, 29(6), 687-711. https://doi.org/10.1002/esp.1064

Marianelli, P., et al. (2005). The deep feeding system of Vesuvius involved in recent violent strombolian eruptions. Geophysical Research Letters, 32(2). https://doi.org/10.1029/2004GL021667

Mayer, C., et al. (2018, October). A comprehensive workflow to process UAV images for the efficient production of accurate geo-information. In IX National Conference on Cartography and Geodesy (pp. 1-8). Ordem dos Engenheiros, Lisbon, Portugal.

Miyabuchi, Y., et al. (2006) Bomb-rich basaltic pyroclastic flow deposit from Nakadake, Aso Volcano, southwestern Japan. J. Volcanol. Geotherm. Res. 155:90–103. https://doi.org/10.1016/j.jvolgeores.2006.02.007

Monticelli, T., & Covelli, N. (1823) Storia de' fenomeni del Vesuvio, avvenuti negli anni 1821, 1822 e parte del 1823, con osservazioni e sperimenti 1823. Aste Bolaffi Editor, Napoli.

Natale, J., et al. (2024). Geomorphic analysis of digital elevation model generated from vintage aerial photographs: A glance at the pre-urbanization morphology of the active Campi Flegrei caldera. Geomorphology, 460, 109267. https://doi.org/10.1016/j.geomorph.2024.109267

Nairn, I. A., & Self, S. (1978) Explosive eruptions & pyroclastic avalanches from Ngauruhoe in February 1975. J. Volcanol. Geotherm. Res. 3(1-2):39-60. https://doi.org/10.1016/0377-0273(78)90003-3

Neri, A., et al. (2026) "Assessing deposit-derived pyroclastic flow hazard at Stromboli (Italy): 1. Reconstruction of the dynamics of the 11 September 1930 event." Journal of Geophysical Research: Solid Earth 131.5: https://doi.org/10.1029/2025JB032568.

Norini, G. et al. (2009) The 16 November 2006 flank collapse of the south-east crater at Mount Etna, Italy: Study of the deposit & hazard assessment. J. Geophys. Res. Solid Earth 114. https://doi.org/10.1029/2008JB005779

Parascandola, A. (1945). L'eruzione vesuviana del marzo 1944, i prodotti piroclastici. Rendiconti Accademia Scienze Fisiche Matematiche di Napoli, Serie IV, 13, 285–305.

Pensa, A., et al. (2023). A new hazard scenario at Vesuvius: deadly thermal impact of detached ash cloud surges in 79CE at Herculaneum. Scientific Reports, 13(1), p.5622. https://doi.org/10.1038/s41598-023-32623-3

article in press

Pioli, L., et al. (2008) The eruptive activity of 28 & 29 December 2002. In: "The Stromboli Volcano: An integrated study of the 2002-2003 Eruption", American Geophysical Union Monograph Series, Calvari S., Inguaggiato S., Puglisi G., Ripepe M. & Rosi M. (Editors), v. 182, 105-116. https://doi.org/101029/182GM10. ISBN 978-0-87590-447-0.

Pistolesi, M., et al. (2011). The 15 March 2007 explosive crisis at Stromboli volcano, Italy: assessing physical parameters through a multidisciplinary approach. Journal of Geophysical Research: Solid Earth, 116(B12). https://doi.org/10.1029/2011JB008527

Risica, G., et al. (2022) Deposit-derived block-and-ash flows: the hazard posed by perched temporary tephra accumulations on volcanoes; 2018 Fuego disaster, Guatemala. J. Geophys. Res. Solid Earth 127:e2021JB023699. https://doi.org/10.1029/2021JB023699

Rittmann, A. (1931). Der Ausbruch des Stromboli am 11 September 1930. Zeits. Vulkanol., 14, 47-77.

Romero, J. E., et al. Volcanic lateral collapse processes in mafic arc edifices: a review of their driving processes, types & consequences. Frontiers in Earth Science, 9, 639825 (2021). https://doi.org/10.3389/feart.2021.639825

Rosi, M., et al. (1993). The 1631 Vesuvius eruption. A reconstruction based on historical and stratigraphical data. Journal of Volcanology and Geothermal Research, 58(1-4), 151-182. https://doi.org/10.1016/0377-0273(93)90106-2

Rosi, M., & Santacroce, R. (1983). The AD 472 "Pollena" eruption: volcanological and petrological data for this poorly-known, Plinian-type event at Vesuvius. Journal of Volcanology and Geothermal Research, 17(1-4), 249-271. https://doi.org/10.1016/0377-0273(83)90071-9

Rosi, M., et al. (2006). A case history of paroxysmal explosion at Stromboli: timing and dynamics of the April 5, 2003 event. Earth and Planetary Science Letters, 243(3-4), 594-606. https://doi.org/10.1016/j.epsl.2006.01.035

Salvatici, T. et al. (2016) From hot rocks to glowing avalanches: Numerical modelling of gravity-induced pyroclastic density currents & hazard maps at the Stromboli volcano (Italy). Geomorphology 273:93–106. https://doi.org/10.1016/j.geomorph.2016.08.011

Sato, H., Fujii, T., & Nakada, S. (1992). Crumbling of dacite dome lava and generation of pyroclastic flows at Unzen volcano. Nature, 360(6405), 664-666. https://doi.org/10.1038/360664a0

Santacroce, R. (1987). Somma-Vesuvius, CNR, Quaderni de la Ricerca Scientifica, 114, Progetto Finalizzato Geodinamica, Monografie Finali.

Scandone, R., et al. (2008). Persistent activity and violent strombolian eruptions at Vesuvius between 1631 and 1944. Journal of Volcanology and Geothermal Research, 170(3-4), 167-180.8 https://doi.org/10.1016/j.jvolgeores.2007.09.014

article in press

Sheridan, M. F., et al. (1981). A model for Plinian eruptions of Vesuvius. Nature, 289(5795), 282-285. https://doi.org/10.1038/289282a0

Skempton, A.W., Hutchinson, J.N. (1969). Stability of natural slopes and embankment foundations. In: Proceedings, 7th. International conference of soil mechanics and foundation engineering, Mexico, State of the Art volume, pp. 291–340.

Stinton, A. J., Cole, P. D., Odbert, H. M., Christopher, T., Avard, G., & Bernstein, M. (2014). Dome growth and valley fill during Phase 5 (8 October 2009–11 February 2010) at the Soufrière Hills Volcano, Montserrat. https://doi.org/10.1144/M39.6

Sulpizio, R., Castioni, D., Rodriguez-Sedano, L. A., Sarocchi, D., & Lucchi, F. (2016). The influence of slope-angle ratio on the dynamics of granular flows: insights from laboratory experiments. Bulletin of Volcanology, 78(11), 77. https://doi.org/10.1007/s00445-016-1069-5

Turchi, A., et al. (2026). Risk awareness characterisation in multi-hazard, high-tourist-interest sites: the case of Stromboli Volcano during the 2019 eruptive crisis (Aeolian Islands UNESCO site, Italy). Submitted to Natural Hazards. https://doi.org/10.1007/s11069-026-08001-3

Yamamoto, T., et al. (2005) Basaltic pyroclastic flows of Fuji volcano, Japan: characteristics of the deposits & their origin. Bull. Volcanol. 67:622–633. https://doi.org/10.1007/s00445-004-0398-y

Zuccarello, F., et al. (2025) Trigger mechanism & propagation dynamics of pyroclastic density currents at basaltic volcanoes. Commun. Earth Environ. 6(1):1-12. https://doi.org/10.1038/s43247-025-02397-9

article in press